Development of a plasma waveguide for high-intensity laser pulses

C. G. Durfee III, J. Lynch, and H. M. Milchberg
Institute for Physical Science and Technology, University of Maryland, College Park, Maryland 20742
(Received 21 July 1994; revised manuscript received 31 October 1994)

We present a comprehensive report on recent experiments [Durfee and Milchberg, Phys. Rev. Lett. **71**, 2409 (1993); Durfee, Lynch, and Milchberg, Opt. Lett. **19**, 1937 (1994)] in which the channeling of intense laser pulses over distances much greater than a Rayleigh length was demonstrated using a two-laser-pulse technique. The first pulse creates a breakdown spark in a gas target, and the expansion of the resulting hot plasma forms a channel which guides a second pulse, injected into the channel after an appropriate delay. Data are presented for channels of 24 Rayleigh lengths (0.7 cm), while pulses have been channeled up to 70 Rayleigh lengths (2.2 cm), with up to 75% of the energy in the injected pulse focal spot coupled into the guide. In spite of the high intensities of the channel beam (here up to 10^{14} W/cm^2), the propagation is linear and should remain so at even higher intensities. Single-mode, multimode, and leaky mode propagation of the channeled beam is observed, with the mode structure depending on the delay and the gas density. Along with these experimental results, we present a model of the laser-gas interaction and the resulting plasma hydrodynamics and calculate beam propagation and mode structure in plasma waveguides. A special property of a plasma waveguide is that the mode structure is wavelength independent, resulting in a wavelength-independent guiding condition.

PACS number(s): 52.40.Nk, 52.35.Mw, 52.40.Db

I. INTRODUCTION

The guiding of intense optical beams in plasmas has applications which include extremely high harmonic generation [1], recombination far UV and soft x-ray lasers [2], and laser-plasma-based charged particle accelerators [3,4]. These applications require laser pulses propagating at high intensity, generally above the ionization threshold of atoms. Although with current laser technology, such intensity can be achieved in a tightly focused beam, the subsequent spreading of the beam due to diffraction imposes a severe limitation on the total interaction length. For a focused Gaussian beam, the interaction length is approximately a confocal parameter $2z_0$, where $z_0 = n\pi w_0^2/\lambda$ is the Rayleigh length, w_0 is the $1/e^2$ intensity radius of the waist, n is the refractive index of the medium, and λ is the vacuum wavelength. There is a tradeoff between the interaction length and the intensity ($I \sim E_p/w_0^2$, where E_p is the pulse energy), since $Iz_0 \sim E_p/\lambda$, a constant.

Intense pulses may be guided in plasmas if the effective refractive index along the optical axis can be increased sufficiently to balance diffraction. The recent development of high peak power (in excess of 10^{12} W) tabletop laser systems [5], capable of generating focused intensities exceeding 10^{18} W/cm^2, has renewed interest in charge-displacement and relativistic channeling mechanisms [6,7] for guiding intense pulses. These two mechanisms [8,9] require extremely high focused laser intensities (in excess of 10^{18} W/cm^2). Recent calculations show that a pulse propagating in the charge-displacement and relativistic regimes is subject to erosion: the leading edge is not focused since forward charge displacement diffracts the beam, canceling the effect of relativistic focusing [10]. The trailing edge is subject to scattering by Raman instabilities [11]. Moreover, there are difficulties in propagating such a powerful pulse to the region of high intensity needed for the onset of self-focusing, since the beam may break up due to filamentation [12] or may be defocused due to the electron density maximum generated along the optical axis resulting from ionization [13].

These difficulties can be avoided when the laser pulse to be guided does not create its own channel. The method described here uses a laser pulse to create a spark in a background gas in the line focus of an axicon lens [14]. The spark plasma expands at the local sound speed, and ion-ion and ion-atom collisions lead to the formation of a shock wave at the boundary between the hot plasma and the neutral or weakly ionized gas on the periphery. The cylindrical expansion of the shock wave results in radially increasing plasma density, thereby forming a waveguide into which a second pulse is injected after a controllable delay. To produce this plasma waveguide, the intensity should be at or above the threshold for multiphoton ionization, a much more modest requirement than for the charge-displacement and relativistic self-focusing mechanisms. Under these conditions, the preformed channel is stable and reproducible, essential for any real applications. This two-pulse technique makes guiding possible in a linear propagation regime closely resembling that in solid optical fibers, for intensities below the threshold for additional ionization or ponderomotive and relativistic self-focusing. The propagating intensity of the pulse (or multiple pulses) may therefore be varied independently. Unlike other dielectric fibers, the plasma fiber supports not only high-intensity pulses, but also wavelengths extending into the soft x-ray region. Moreover, as the shock wave expands, the curvature of the density profile relaxes and the size of the lowest-order guided mode increases. This allows the relative delay of the two pulses to be adjusted to optimize the matching of

the input beam size to the lowest-order mode of the channel, resulting in high input coupling efficiencies. The channel diameter, and length, the depth of the refractive index difference, and the central plasma density can be varied over a wide range. Even glass optical fibers do not allow such a ready adjustment of parameters.

Previous work has shown that laser-produced sparks can produce plasma density minima on axis. For example, Askar'yan and Tarasova [15] demonstrated reduced scattering of an electron beam injected into a spark produced with a 30-J, 30-ns laser pulse, due to the decreased plasma density in the path of the beam. Johnson and Chu [16] measured the shock wave profile created during the interaction of 150-ns CO_2 laser pulses with 30 Torr of helium. The observed refraction of the unstable resonator beam was interpreted as evidence of lensing of the trailing part of the pulse from the plasma density profile created earlier in the pulse. In other early work, it was established that a plasma density minimum could refract a beam. For example, Molen, Kristiansen, and Hagler [17] created such a plasma with a discharge, and Amherd and Vlases [18] used a theta pinch. In both experiments the plasma was probed with large diameter beams (the Rayleigh length was greater than the plasma length), and no increase in the propagation distance was shown.

The work presented here is a demonstration of whole beam guiding of intense optical pulses over distances much greater than a Rayleigh length [19]. Multiple foci due to self-focusing of long pulses [20,21] and short pulses [6,22] have been reported, but in those cases the beams were not confined to a small transverse size throughout the interaction length. The data presented here are for channels approximately a centimeter in length ($\sim 24 z_0$) while somewhat less stable channels as long as 2.2 cm ($\sim 70 z_0$) have also been generated (using an axicon of shallower angle, see Sec. V A). Thus a very high product of the intensity and the interaction length is achieved, opening up a previously inaccessible regime of laser interaction with plasmas, ions, and atoms.

The remainder of the paper is organized as follows: In Sec. II, processes that contribute to the formation of the plasma waveguide are summarized. Section III addresses the issues relating to beam propagating in the waveguide. Section IV describes initial experiments which showed that a gas breakdown in a laser focus produces a short channel with a density profile favorable for lensing a beam. In Sec. V, the use of an axicon lens to produce a long plasma channel is described, followed by a description and discussion of the resulting guiding experiments.

II. SEEDED AVALANCHE BREAKDOWN AND SHOCK WAVE FORMATION

The plasma waveguide is formed through the hydrodynamic evolution of a laser-produced plasma in a gas. The initial plasma is formed through a seeded avalanche breakdown. The laser intensities used here (2×10^{13}–5×10^{14} W/cm^2) are sufficient for direct multiphoton ionization of all or a substantial fraction of the atoms in the gases used (Xe, Ar, N_2). Since the pulse duration is longer than the average electron-ion collision time $\tau_{ei}\sim 1/\nu_{ei}$, the laser field heats the plasma through inverse bremsstrahlung (IB), leading to further ionization through collisions. This collisional ionization occurs either during or after the pulse, depending on the electron temperature, ionization potential, and gas density. Since $N_e/N_{cr}\sim 10^{-2}$–10^{-3}, parametric heating mechanisms, in which waves in the plasma are driven by the laser, are negligible compared with inverse bremsstrahlung absorption. The IB heating of the plasma aids in the formation of the waveguide, as it serves to drive the shock expansion in the presence of thermal and hydrodynamic losses. The time scale for hydrodynamic evolution of the channel is $\tau_{ch}=w_0/c_s$, where $c_s=(\langle Z\rangle \kappa_B T_e/m_i)^{1/2}$ is the sound speed in the heated plasma, and $\langle Z\rangle$, κ_B, T_e, and m_i are the average ion charge, the Boltzmann constant, the electron temperature, and the ion mass, respectively. If the pulse duration is longer than τ_{ch}, heating occurs during the plasma expansion, resulting in a profile which is too broad to act as a waveguide for small low order modes. A computer code, developed to calculate the response of a gas to irradiance by intense laser beams, will first be described. The sections following will summarize the time and length scales characteristic of the experimental parameter ranges.

A. Computer simulations of laser-gas interactions

For an ideal gas with constant specific heats, the evolution of a strong shock wave initiated from a point or a line source can be solved analytically [23]. In a real gas or plasma, the evolution of the structure of a strong shock wave is more complicated. To understand in more detail the dynamics of the interaction of high-intensity pulses with gases and the resulting shock formation, a plasma dynamics code was developed [19]. The one-fluid equations [24] are used for mass, momentum, and energy conservation since the plasma is charge neutral everywhere except at a thin layer (of thickness of approximately a Debye length, λ_D) at the shock front. Field ionization (using tunneling rates calculated by Ammosov, Delone, and Krainov [25]), inverse bremsstrahlung heating of the electrons, electron-ion thermal coupling, collision-based ionization and recombination, and thermal conduction (both gradient driven and flux-limited flow) are coupled to the hydrodynamics. Ionization and recombination are included in the energy balance, while radiation is neglected since it contributes negligibly.

Figure 1(a) shows a calculation of time dependent electron density profiles for 100 Torr of argon (background density $N_0\sim 3.5\times10^{18}$ cm^{-3}) subjected to a Gaussian in space and time pulse (100-ps FWHM, peak intensity 5×10^{13} W/cm^2, spot size $w_0=10$ μm), where the development of a channel favorable for guiding is seen. Figure 1(b) compares the peak average ionization level ($\langle Z\rangle$) achieved at 30 and 100 Torr. At 30 Torr, ionization during the laser pulse is mostly attributable to field ionization, while electrons are heated by inverse bremsstrahlung. The plasma is strongly out of ionization equilibrium: collisional ionization takes place after the laser pulse, on a time scale of a few nanoseconds. For higher back-

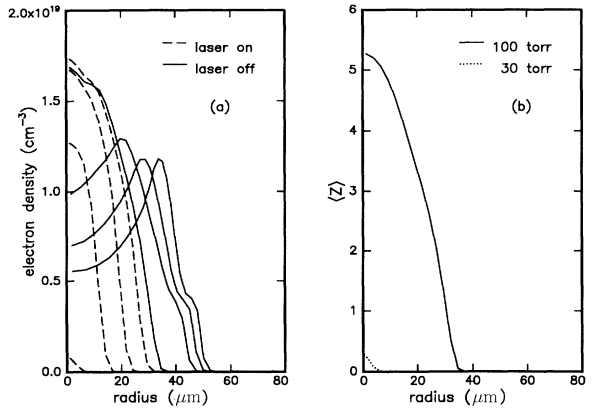

FIG. 1. Plasma dynamics calculation for a peak intensity 5×10^{13} W/cm^2, Gaussian (in time and space) laser pulse with FWHM duration $\tau_p=100$ ps (peak at 120 ps and termination at 240 ps), focal spot size $w_0=10$ μm, and $\lambda=1.064$ μm, showing (a) evolution of the electron density profile for an initial density of 100 Torr ($N_0\sim3.5\times10^{18}$ cm^{-3}) argon, and (b) peak average ionization level $\langle Z\rangle$ for argon at 30 and 100 Torr. For (a), the time interval between dashed lines (laser on) is 50 ps, with 500 ps between solid lines (laser off).

ground densities, avalanche ionization contributes more significantly to the breakdown, as shown in the collisionally enhanced $\langle Z\rangle$ profile at 100 Torr.

The calculations illustrate the role of thermal conduction in the evolution of the plasma density profile. If there is electron density ahead of the shock wave (due to diffusion, ionizing radiation from the plasma, or ballistic transport), thermal conduction heats those electrons, depleting energy from the plasma column. A thermal precursor wave [seen in Fig. 1(a)] propagates in advance of the shock wave, in which the heated electrons further ionize the gas collisionally.

B. Inverse bremsstrahlung heating

The rate of expansion of the shock wave and the final ionization level are strongly dependent on the degree of laser heating of the electrons. The scaling of the average electron energy change with pulse duration, pulse energy, and laser wavelength for inverse bremsstrahlung can be estimated using the Lorentz plasma model. In the absence of losses, this model gives [26] a heating rate $d\varepsilon/dt=(e^2E_0^2/2m_e\omega^2)[\omega^2/(\omega^2+\nu_m^2)]\nu_m\approx2U_P\nu_m$, for $\nu_m\ll\omega$ (satisfied for the experimental conditions of gaseous density plasma), where e and m_e are the electron charge and mass, ν_m is the collision rate for momentum transfer, $U_P=\frac{1}{4}e^2E_0^2/m_e\omega^2\approx9.33\times10^{-14}I$ (W/cm^2) λ^2 (μm) is the ponderomotive potential, and E_0, I, and ω are the laser electric field, intensity, and frequency. In this limit, an electron acquires on average an energy of $\Delta\epsilon=2U_P$ per collision.

Consider first the case of IB heating resulting from electron-atom collisions. The interaction is dominated by the polarization force so the electron-atom cross section σ_{ea} varies as $1/v$ (where v is the relative velocity between the electron and atom). The collision rate $\nu_{ea}\sim N_a\sigma_{ea}v$ is then independent of velocity, and the expression for the heating rate given by the Lorentz plasma model is accurate. Experimental measurements of the cross section for noble gases [27] show that over an electron energy range of 4–40 eV, $\nu_{ea}\approx6.1\times10^{-7}N_a$ (cm^{-3})s^{-1}. For $N_a=10^{18}$ cm^{-3}, the characteristic heating time scale is $t^*=1/\nu_{ea}\approx1.7$ ps. The net electron temperature rise due to electron-atom IB heating for a square pulse of duration τ_p is $\kappa_B\Delta T_e\approx\frac{2}{3}\Delta\epsilon\approx(\frac{4}{3})U_P\nu_{ea}\tau_p$. Since $U_P\propto\lambda^2E_p/\tau_p$, where E_p is the pulse energy, $\Delta T_e\propto E_p\lambda^2$, and is independent of the pulse duration.

For electron-ion collisions, the Coulomb collision cross section is strongly dependent on the electron velocity, and the collision rate must be modified to include the effect of the quiver velocity of the electron in a strong laser field. An effective collision frequency has been calculated [28] in the high-field limit $U_p\gg\kappa_BT_e$, where the ponderomotive quiver velocity dominates the mean thermal velocity. Here the conditions may satisfy $U_P\gg\kappa_BT_e$ early in the heating, but the electron thermal energy may rise enough that $U_P\ll\kappa_BT_e$. The intermediate range is modeled here by using an effective temperature $T_{\rm eff}=\kappa_BT_e+U_P$, yielding an effective collision frequency $\nu_{ei}(T_{\rm eff})\sim4\pi\langle Z\rangle^2N_ie^4\ln\Lambda_{ei}/m_e^{1/2}T_{\rm eff}^{3/2}$, where $\ln\Lambda_{ei}$ is the Coulomb logarithm. The heating process may then be understood qualitatively by integrating the equation for $d\varepsilon/dt$ for a square laser pulse of constant intensity, using $\nu_m\ll\omega$ and assuming that the Coulomb logarithm $\ln\Lambda_{ei}$ is slowly varying, giving

$$\kappa_BT_e(t)=U_P[(\alpha\nu_Pt+1)^{2/5}-1]\ . \tag{1}$$

Here $\nu_P=\nu_{ei}(U_P)$ is the high-field collision rate, $\alpha=\frac{10}{3}$, and it has been assumed that $\kappa_BT_e(t=0)\ll U_P$. A characteristic heating time $t^*=1/\alpha\nu_P$ separates two regimes of IB heating. For typical experimental parameters of $N_e=10^{18}$ cm^{-3}, $\lambda=1.064$ μm, $Z=1$, $\ln\Lambda_{ei}\approx10$, and $I\approx10^{14}$ W/cm^2, the heating time is $t^*\approx90$ fs. This is much less than the pulse duration in the present experiments ($\tau_p=100$ ps), which are therefore in the long-pulse regime ($t\gg t^*$). By contrast, many high-intensity laser experiments ($\tau_p\le1$ ps, $I\ge10^{15}$ W/cm^2) are in the short-pulse regime ($t\ll t^*$). For example, for the above conditions and $I\approx10^{16}$ W/cm^2, t^* is approximately 90 ps.

The scaling of the temperature rise is very different in the two regimes. In the short-pulse regime, Eq. (1) reduces to $\kappa_BT_e(t)\approx\frac{2}{5}U_P(t/t^*)$, or $\Delta T_e\propto\tau_p^{3/2}/\lambda E_p^{1/2}$, using $\nu_P\propto U_P^{-3/2}\propto(E_p\lambda^2/\tau_p)^{-3/2}$. The plasma is heated to a lesser degree with larger pulse energies due to the inverse velocity dependence of the scattering cross section, while longer pulses are more effective in heating. In the long-pulse regime, $\kappa_BT_e(t)\approx U_P(t/t^*)^{2/5}$ or $\Delta T_e\propto\lambda^{4/5}E_p^{2/5}$, dependent only on pulse energy and independent of pulse duration. As an indication that longer pulses can be much more effective in heating the plasma, consider again the laser and gas conditions used to calculate t^* above. For $\tau_p=100$ ps and $I\approx10^{14}$ W/cm^2 ($U_P=10$ eV), $\tau_p/t^*\approx1000$, and $\Delta T_e\approx170$ eV. However, a pulse with the same energy but with $\tau_p=1$ ps

(such that $I \approx 10^{16}$ W/cm^2 and $U_P = 1$ keV) gives $\tau_p / t^* \approx 0.01$ and $\Delta T_e \approx 5$ eV.

The experiments reported here are in a density range (> 5 Torr) in which electron thermalization occurs over a time much shorter than the laser pulsewidth ($\tau_p = 100$ ps). The electrons approach a Maxwellian distribution over a few mean electron-electron collision times $1/\nu_{ee}$. For $N_e = 10^{18}$ cm^{-3} and $T_e = 50$ eV, $1/\nu_{ee} \approx 4.5$ ps. Spatial gradients in the electron temperature in the plasma column are also quickly reduced due to fast thermal conduction resulting from these collisions. For a temperature gradient scale length L the conduction time scale τ_c can be estimated as $\tau_c \sim N_e L^2/(\kappa/\kappa_B) \sim (L/\lambda_{ee})^2 (1/\nu_{ee})$, where κ is the thermal conductivity and λ_{ee} is the electron-electron mean free path. For $N_e = 10^{18}$ cm^{-3} and $T_e = 50$ eV, $\lambda_{ee} = 13$ μm, and, for $L = 10$ μm, $\tau_c \approx 200$ fs. During a laser pulsewidth of $\tau_p = 100$ ps under these conditions, heat diffuses over a distance of approximately $L \sim \lambda_{ee}(\tau_p \nu_{ee})^{1/2} \approx 200$ μm. Thus, during the 100-ps laser pulse of the present experiment, the electron temperature is essentially uniform across the plasma column (which is usually less than 50 μm in radius during guided pulse injection), and there is an appreciable amount of thermal conduction along the axis of the column.

Electrostatic confinement of the electrons allows heat flux only in the plasma column and weakly ionized plasma outside the shock front. The plasma densities of these experiments are such that the electrons are retained in the focal region due to electrostatic forces, leading to charge neutrality except in a thin layer whose thickness is on the order of a Debye length $\lambda_D = (\kappa_B T_e / 4\pi N_e e^2)^{1/2}$ at the boundary between the ionized plasma column and the background (weakly ionized) gas. For $N_e \approx 10^{18}$ cm^{-3} and $T_e \approx 50$ eV, $\lambda_D \approx 50$ nm. Collisional ionization at the plasma periphery during or after the laser pulse and ballistic electron transport serve to extend the heat flow radially.

C. Seeded avalanche breakdown

The increase in electron temperature due to inverse bremsstrahlung heating leads to collisional ionization. The increase in electron density due to collisional ionization follows $dN_e/dt = N_e(N_0 - N_e)S(T_e)$, where the collisional ionization rate S is averaged over the electron velocity distribution, and $N_0 = N(0)$ is the ion or atom density at $t = 0$. For a Maxwellian electron distribution and $U_p/kT_e \ll 1$, the rate for ionization out of the ground state of a hydrogenlike atom of ionization potential U_I (more complex atoms or ions can be approximated by using an effective Z) is approximately [29] $S(T_e) = 10^{-5}(T_e/U_I)^{1/2} \exp(-U_I/T_e)/[U_I^{3/2}(6.0 + T_e/U_I)]$ cm^3/s, with T_e and U_I in eV. The high energy tail of the electron distribution function allows for fractional ionization of high ion stages. An approximate time for electron density buildup is $\tau_e \sim (N_0 S(T_e))^{-1}$. This does not account for collisional ionization out of excited states, which would reduce τ_e. For neutral argon (ionization potential $U_I = 15.76$ eV) at $N_0 = 10^{18}$ cm^{-3} and $T_e = 50$ eV, $\tau_e \approx 45$ ps. If $\tau_e > \tau_p$, the electrons are heated without losing energy to ionization during the pulse, and ionization takes place after the pulse. If $\tau_e < \tau_p$, ionization occurs during the pulse, limited mainly by the time required to heat the electrons to some fraction of U_I. The time taken to reach saturation of a particular stage of ionization, τ_{sat}, may be estimated by setting $N_e = N_0/2$, yielding $\tau_{sat} = \tau_e \ln[(N_0 - N_{e0})/N_{e0}]$, where N_{e0} is the initial density of electrons.

For avalanche breakdown of a pure neutral gas with a high U_I, N_{e0} can be very small, and the time to saturation τ_{sat} can be many times τ_e. The resulting breakdown fluctuates with variations in the input pulse energy which lead to large variations in N_{e0}. If, however, N_{e0} is already large, τ_{sat} is of the same order as τ_e. An added gas of lower U_I (such as xenon, which has $U_I = 12.1$ eV) provides a stable source of free electrons to seed a stable avalanche breakdown of the main gas. If the Debye length for these seed electrons is smaller than the focal spot size r_0, diffuse electron losses from the focal region are limited by space charge forces. For a plasma column in a line focus with $r_0 = 2$ μm and $T_e = 50$ eV, this occurs at a transition electron density $N_{tr} = \kappa_B T_e / 4\pi e^2 r_0^2 \approx 10^{16}$ cm^{-3}, so that in the experiments described in this paper ($N_e > 10^{18}$ cm^{-3}) diffusion is strongly dominated by space charge.

D. Microscopic picture of shock wave formation

From a fluid perspective, a shock wave forms when a disturbance propagates at a speed greater than the local sound speed [30]. Here the heated electrons pull the cooler ions radially outward, and the plasma expands at the local ion sound speed $c_s = (\langle Z \rangle \kappa_B T_e / m_i)^{1/2}$. The plasma expansion speed is much greater than the sound speed c_0 in the surrounding weakly ionized gas, even at electron temperatures as low as 1 eV (where $c_s/c_0 \approx 5$). The ions in the expanding front collide with both ions and atoms in the relative cool weakly ionized gas on the periphery of the plasma column. On a microscopic scale, these collisions lead to a density buildup at the interface between the two regions, forming the shock front. The plasma column periphery (beyond the shock radius) is partly ionized by prompt UV emission from the heated plasma, and contains electrons that have reached this region by diffusion or ballistic transport. Heat conduction to electrons on the periphery leads to additional collisional ionization there, resulting in a thermal ionization precursor wave. The ion-ion mean free path λ_{ii} is approximately the minimum width of the shock (the shock width will generally be larger than λ_{ii} due to thermal diffusion), while the effective shock growth rate is $\nu_{ii} \sim c_s/\lambda_{ii}$. For argon ($m_i = 40$ a.u.) at $N_i = 10^{18}$ cm^{-3}, $T_e = 50$ eV, expanding plasma ion charge $\langle Z_1 \rangle = 5$, and a background plasma ion charge $\langle Z_2 \rangle = 1$, $c_s \approx 2.5 \times 10^6$ cm/s, $\lambda_{ii} \approx 2.5$ μm, and $1/\nu_{ii} \approx 100$ ps, and the expansion time scale for the plasma column is $\tau_{ch} \sim r_0/c_s \approx 0.5$ ns for an initial radius $r_0 = 10$ μm. The ion temperature plays a small role in the ion-ion impact velocity: it remains low during the characteristic expansion time τ_{ch}, since thermal energy is transferred to the ions through collisions with the elec-

trons at a rate $\nu_E = 2(m_e/m_i)\nu_{ei}$. For the above conditions, $1/\nu_E \approx 8$ ns. Shock evolution is faster for higher density and lighter ions: for the same temperature $\langle Z_1 \rangle$ and $\langle Z_2 \rangle$, but with nitrogen at density $N_i = 10^{19}$ cm^{-3}, $c_s \approx 4\times10^6$ cm/s, $\lambda_{ii} \approx 0.25$ μm, and $1/\nu_{ii} \approx 6$ ps.

Ion-atom collisions also play a role in the formation of the shock wave, especially when there is little precursor ionization. The ion-atom collision cross section σ_{ia} (resulting mainly from the polarization force) depends weakly on the impact energy if it is greater than a few eV. Using an experimentally measured value [31] of $\sigma_{ia} \approx 2.5\times10^{-15}$ cm^2 for argon, the mean free path for ion-atom scattering is $\lambda_{ia} \approx 1/(N_a\sigma_{ia}) \approx 4$ μm at $N_a = 10^{18}$ cm^{-3}, and $1/\nu_{ia} = \lambda_{ia}/c_s \approx 270$ ps (for $c_s = 1.5\times10^6$ cm/s).

At low density, the shock thickness may be larger than the intended channel spot size. The requirement that $\lambda_{ii} < w_0$ yields a condition on the minimum density N_{sh} for the formation of a shock wave on a scale that will allow the channeling of a spot size w_0: $N_{sh} < 1/w_0\sigma_{ii}$. For $w_0 = 10$ μm, $T_e = 50$ eV, $\langle Z_1 \rangle = 5$, N_{sh} is approximately 2.5×10^{17} cm^{-3}.

III. OPTICAL GUIDING IN PLASMAS

A. Guiding condition for the plasma waveguide

For a laser beam to be confined in a dielectric waveguide at constant size, the wave front at the optical axis must be retarded more than at the beam periphery to compensate for the outward curvature of diffraction. A Gaussian beam passing through a length δz of a graded index waveguide with refractive index difference Δn between the center and beam radius w_0 will experience focusing due to the index profile and defocusing due to diffraction. The focusing contribution to the beam radius of curvature is $R_F \approx w_0^2/(2\Delta n \delta z)$. The diffractive defocusing contribution is $R_D = \delta z(1 + z_0^2/\delta z^2) \approx z_0^2/\delta z$. A Gaussian beam will maintain a flat phase front (and thus a constant beam size) when $R_F = R_D$, or

$$\Delta n^{\min} = \frac{\lambda^2}{2\pi^2 w_0^2 n_0^2} = \frac{1}{k z_0} , \tag{2}$$

where $k = 2\pi n_0/\lambda$, and n_0 is the refractive index at $r = 0$. Even for small beam sizes, $\Delta n^{\min}$ is not very large $\Delta n^{\min} \approx 6\times10^{-4}$ for $w_0 = 10$ μm, $\lambda = 1.064$ μm, and $n_0 \approx 1$).

In an unmagnetized plasma, the refractive index is $n^2 = 1 - N_e/N_{cr}$, where $N_{cr} = m_e\omega^2/4\pi e^2$ is the critical electron density ($N_{cr} \approx 10^{21}$ cm^{-3} for $\lambda = 1.064$ μm). For the underdense plasma conditions of these experiments, $N_e/N_{cr} \approx 10^{-2}$–$10^{-3}$, so $n \approx 1 - \frac{1}{2}N_e/N_{cr}$. The guiding condition (2) determines the minimum electron density difference necessary to channel a beam of spot size w_0:

$$\Delta N_e^{\min} = \frac{1}{r_0 \pi w_0^2} , \tag{3}$$

where $r_0 \approx 2.82\times10^{-13}$ cm is the classical electron radius. For $w_0 = 10$ μm, $\Delta N_e^{\min} \approx 10^{18}$ cm^{-3}. This corresponds to a minimum background pressure requirement of about 30 Torr of monatomic gas at single ionization. Condition (3) is exact for a parabolic profile, and is also quite accurate for other channel profiles [32]. Note that the density difference determines the spot size that may be channeled, independent of the wavelength. In fact, it can be shown that the eigenmodes of a general plasma waveguide are wavelength independent [33]. Therefore, if short wavelength light is generated in the channel, it will be guided along with the optical pump beam if the two beams are the same size. In the present configuration, the guided light frequency is well above the dominant resonance frequencies ω_0 of the ions, so their contribution to the index profile is small. The refractive index contribution of neutral Xe at $N_a = 10^{18}$ cm^{-3} and $\lambda = 1$ μm is [34] $n - 1 \approx 2.5\times10^{-5}$. The ions, with their lower polarizability, contribute even less than the atoms. By comparison, the electron contribution is $1 - n \approx 5\times10^{-4}$.

B. Mode properties of plasma waveguides

The mode properties of the plasma waveguide may be described in terms of three simple models: the infinite profile, in which the plasma density increases with radius to at least the critical density, the finite profile, in which the plasma density reaches a (subcritical) maximum and is constant beyond that point; and the real profile, which resembles those shown in Fig. 1, in which the density increases with radius, reaches a maximum, then falls to zero beyond the shock front.

For the infinite profile, there are only bound modes. Consider the special case of a parabolic plasma density profile $N_e(r) = N_e(0) + N_{cr}(r/a)^2$, where a is a curvature parameter. Applying the guiding condition (3) to this profile shows that an input beam of radius w_0 should be guided at constant size if $w_0 = (a\lambda/\pi)^{1/2}$ or $a = z_0$, so that the Rayleigh length of the guided beam is equal to the curvature parameter of the channel. For this profile, the channel eigenmodes are Laguerre-Gaussian functions, similar to the free space modes [35], except that the phase fronts of the eigenmodes are flat. The propagation constant is

$$k_{ch}^2 = k_{p,m}^2 = k_0^2 n_0^2 \left[1 - \frac{4}{k_0^2 n_0 w_0^2}(2p + m + 1) \right] , \tag{4}$$

where p and m are the radial and azimuthal mode indices. Each of these eigenmodes propagates with a different phase velocity $\omega/k_{p,m}$. Aside from the requirement that $\omega > \omega_{p0}$, where ω is the input laser frequency, there is a more restrictive mode cutoff $(4/k_0 w_0^2)(2p + m + 1) < k_0 n_0$, which means that the mode must lie within an underdense region. For example, the critical density point must lie outside of the $1/e$ point of the lowest order (Gaussian) mode. Although the eigenmode profiles are wavelength independent, this cutoff condition is wavelength dependent.

In the finite profile, the maximum density difference restricts further the number of bound modes that may

propagate. A code has been developed to calculate these eigenmodes numerically [33]. A simple model of the finite profile is a parabolic core (for $r < r_m$) and a cladding of constant density [$N_e(r_m)$ for $r > r_m$]. Since the modes away from cutoff are similar to those calculated for the infinite parabolic channel, the eigenmodes supported by a maximum density difference $\Delta N_e = N_e(r_m) - N_{e0}$ satisfy, using Eq. (4),

$$\Delta N_e(p,m) > \frac{(2p+m+1)^2}{r_0 \pi r_m^2} . \quad (5)$$

A mode that is just below the cutoff condition is confined, but with an exponential damping length that extends well beyond r_m. Equation (5) does not account for the difference between these modes and those calculated for the infinite case.

As seen in Fig. 1, the real plasma density profiles drop to zero beyond the shock front. A beam initially in the channel with an exponential damping length greater than the shock width will lose energy due to tunneling. The wave number spectrum of the real channel is not discrete since the waves are not bound. For waves that are strongly damped before the shock front, the mode profile is essentially the same as in an infinite channel, but the eigenvalue has an imaginary component that accounts for the leakage during propagation along the channel. This quasibound wave form is sometimes called a leaky mode [36]. These radiating modes, although not bound, do not diverge as quickly as free space modes. For a waveguide that can only support a finite number of bound modes, there is a spatial transient regime in which leakage occurs, after which only the eigenmodes survive. The spatial transient regime can be important when the channel lengths are relatively short, as in the experiments presented here.

Nonlinear electronic polarizabilities are not expected to affect the beam propagation significantly. From Eq. (2), the change in channeled spot size with an incremental change δn in the refractive index due to nonlinearity is $\delta w_0 \approx -(\delta n / 2\Delta n) w_0$. As an upper limit, consider a channel that guides a $w_0 = 10$-μm spot at constant size ($\Delta N_e \approx 10^{18}$ cm^{-3}) with the nonlinear response of neutral xenon [34] at density 3×10^{18} cm^{-3}. For an intensity of 10^{14} W/cm^2, the spot size change is only $\delta w_0 \approx 5 \times 10^{-4} w_0$.

Additional ionization occurring during the guided pulse may also affect the guiding properties, but since the channel is usually formed by collisional ionization (which is very efficient compared with multiphoton ionization [33]), a short pulse must be very intense to change the electron density profile sufficiently to modify the guided mode profile. Figure 2 demonstrates the effect of injection (after 2-ns delay) of a 10^{17}-W/cm^2, 100-fs pulse into a plasma channel produced in 150 Torr of N_2 by a 5×10^{13}-W/cm^2, 100-ps pulse. It is seen that the short, intense pulse has a negligible effect on the electron density profile and degree of ionization since the collisionally ionized plasma resulting from the first pulse is dominated by He-like ions. At sufficient gas density, collisional ionization is very efficient for long pulses, resulting in a much higher average level of ionization than could be achieved by field ionization. Alternatively, suppose that the level of ionization resulting from the first pulse is low. If the channeled intensity is sufficient to strip the ions to a tightly bound core such that the additional ionization is uniform across the beam, the gradients of the channel profile will be unaffected. For intense pulses that are of sufficiently long duration that the ponderomotive force on the electrons causes ion motion during the pulse (not the case in the present experiments), the mode structure should be affected, leading to coupling between modes. Note that linear propagation is not required for guiding, and channel guiding should also work well at the high intensities of charge displacement and relativistic self-focusing, and even promote their occurrence.

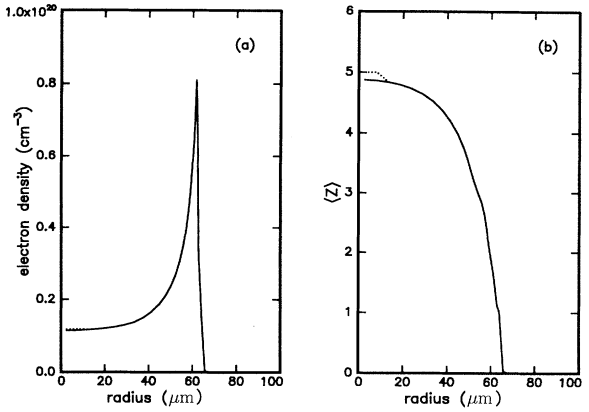

FIG. 2. (a) Calculation of the electron density channel in 150-Torr N_2 after 2-ns delay produced by peak intensity 5×10^{13} W/cm^2, $\lambda = 1.064$ μm, 100-ps pulse just before (——) and after (. . . .) injection of a 10^{17}-W/cm^2, $\lambda = 1$ μm, 100-fs pulse. (b) Corresponding plots of average ionization level $\langle Z \rangle$.

IV. SHORT CHANNEL EXPERIMENTS

A. Laser system and delay calibration

The objective of the first set of experiments was to demonstrate that a laser pulse focused in a gas can produce an index profile appropriate for the guiding of a second laser pulse. These experiments made use of a pump-probe technique in which two pulses were focused through the same lens. The first (pump) pulse was used to form the plasma; the second (probe) pulse was then focused with variable delay into the plasma. The laser system used for the experiments [37] (see Fig. 3) is a tabletop high-power Nd:YAG (yttrium aluminum garnet) system ($\lambda_0 = 1.064$ μm). A mode-locked oscillator provides 100-ps seed pulses at a repetition rate of 76 MHz. This beam is passed through a pulse slicer (PC_1) which selects pulses at 10 Hz for a flashlamp-pumped regenerative amplifier (RGA) and a double-pass power amplifier (PWA) which produces up to 250 mJ of energy. The unstable resonator cavity of the RGA contains an internal spatial filter, which generates a near-Gaussian output mode and results

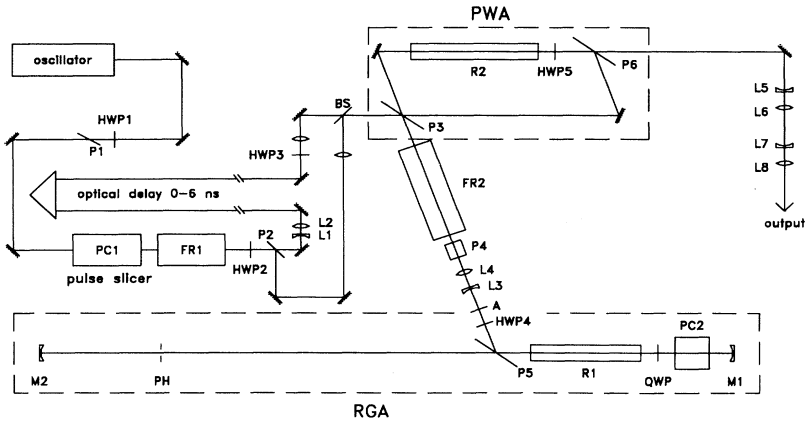

FIG. 3. Nd:YAG regenerative amplifier (RGA) and power amplifier (PWA) laser system. Symbols: half-wave plate (HWP), quarter-wave plate (QWP), polarizer (P), Pockels cell (PC), beamsplitter (BS), lens (L), apodizer (A), mirror (M), Faraday rotator (FR), pinhole (PH), and laser rod (R).

in automatic output beam spatial overlap when the RGA is injected with two input pulses. Depletion of gain in the RGA (over many passes) and gain saturation the PWA (on the second pass) results in a low level of shot-to-shot energy fluctuations (around 3%).

In these experiments, two seed pulses were injected into the RGA to build up simultaneously, one of which passed through a computer-controlled delay line (6 ns) to adjust the relative delay. Ejecting the pulses in the order opposite to which they were injected allowed for a second range of delay (5.5–8 ns). A streak camera monitoring the second harmonic was used to calibrate the delay zero point. The total energy in the two pulses (E_1+E_2) was controlled by adjustment of the pumping level of the PWA (through adjustment of the flashlamp voltage). The output energy ratio (E_1/E_2) was controlled by adjusting the relative seed pulse energies and monitoring the output with a fast photodiode (500-ps risetime) connected to a transient digitizer (750-MHz bandwidth). Careful alignment of the delayed input beam ensured that throughout the full travel of the delay line a constant E_1/E_2 was maintained.

The pulse duration ($\tau_p=100$ ps) used in these experiments is well suited to the time scales discussed above for plasma formation and shock wave evolution. In the presence of conduction and ionization losses and energy expended on hydrodynamic motion, it is necessary to deposit sufficient thermal energy in the plasma to drive the shock wave. Pulses that are short compared to the characteristic time for heating ($\tau_p < t^*$, see Sec. II B) do not effectively heat the plasma after ionization. At the other extreme, laser pulses longer than the hydrodynamic time scale ($\tau_p > \tau_{ch}=r_0/c_s$) continue to heat the plasma as it expands, leading to broad electron density profiles that are unsuitable for guiding small spot sizes. An optimum pulse duration is of order $1/\nu_{ii}$ (typically $\sim 10-100$ ps for the parameters in these experiments), shorter than or comparable to the shock formation time scale and well within the long-pulse heating regime ($\tau_p \gg t^*$ in Sec. III B).

B. Optical diagnostics

Figure 4 is a schematic of the experimental arrangement and the optical diagnostics. The laser output, containing pump and probe pulses, was first gently expanded with a diverging lens (L_1), then focused at $f/10$ with an aplanatic lens ($L_2, f=250$ mm) inside a backfilled chamber filled with xenon (Xe), argon (Ar), or nitrogen (N_2) at pressures of 10–100 Torr. Side images of recombination emission (fluorescence) and scattered laser light from the plasma region were collected (at an angle of 52° to the principal optical axis) to record the changes in spark length that occurred when the second pulse was injected into the plasma. Lenses L_3 and L_4 relayed the light from the focal region out of the chamber, projecting an image onto a charge-coupled device camera (CCD_1) synchronized with the 10-Hz laser trigger. Fluorescence was observed using an IR blocking filter along with color filters to increase the resolution by limiting the chromatic aberration. A blue-pass filter discriminated in favor of light emitted during earlier stages of the plasma recombination, resulting in an image showing sharper features. To view the much weaker scattered laser light, a 3-nm bandpass filter centered at $\lambda=1.064$ μm was used to

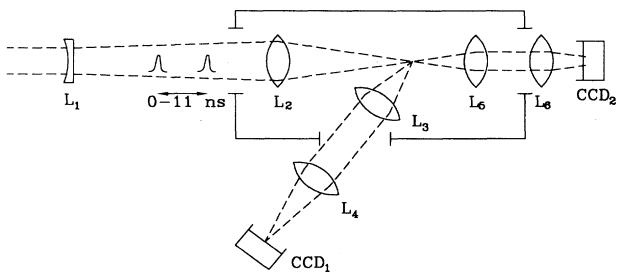

FIG. 4. Short channel experiment and diagnostics.

block plasma self-emission. Another aplanatic lens along the principal optical axis (L_5) recollimated the beam at $f/3$ and was used to monitor the scattering of the probe pulse from the plasma for different delay positions. For these observations, the energy of the probe was reduced to lessen its influence on the plasma. The video output of both CCD cameras was digitized (at eight-bit resolution) with a personal computer-based frame-grabber board. Accumulated images could then be subtracted pixel by pixel for pump-probe measurements and for subtraction of background images. Since both pulses were of the same polarization, polarizers could not be used to observe the second pulse alone. Instead, CCD_2 first integrated the light from both pulses. Subtracted from this double-pulse image was an image resulting from a single pulse with pulse energy $E_s = E_1$ (see below), which resulted in an image of the probe pulse alone. Care was taken to ensure that the single pulse energy and mode shape as the pump pulse. The upper limit of the energy ratio was $E_1/E_2 \approx 7$, both for maintaining an acceptable signal-to-noise ratio in the subtraction and to avoid distortion of the probe pulse that result if the pump pulse saturates the power amplifier.

C. Results and discussion

Figure 5 shows a sequence of spark fluorescence images (CCD_1) for various delays τ_d between the pump and probe pulses, for N_2 at 60 Torr, $E_1 = 70$ mJ, and $E_2 = 70$ mJ (the pulse peak intensity is 4×10^{14} W/cm^2, the spot size is $w_0 = 10$ μm). As τ_d is increased, the spark becomes longer in the direction *away* from the focusing lens. At still longer delays, a gap forms within the elongated region, and the separation of an emerging secondary peak increases with τ_d. At a sufficiently long delay, the second peak disappears (not shown in Fig. 5). Laser scattering images collected with the 3-nm bandpass filter (Fig. 6, Xe at 30 Torr) show peak structure similar to the fluoresecence images. These images are sharper, since the laser light is promptly scattered from the plasma. The laser scattering, however, was too weak to measure with this CCD camera for nitrogen and argon at this pressure. Fluorescence images are more diffuse because the recombination emission takes place over tens of nanoseconds. Figure 7 shows lineouts of fluorescence images at selected delay positions for 30 Torr of N_2 [Fig. 7(a)], Ar [Fig. 7(b)], and Xe [Fig. 7(c)], respectively, all for the same laser conditions as in Figs. 5 and 6. Note that the spark lengthening begins at later delay times τ_{d0} for the heavier gases: $\tau_{d0} \approx 1.3$, 3, and 5 ns for N_2, Ar, and Xe, respectively, consistent with the decrease of sound speed with ion mass.

The appearance of the second spark can be explained as an oscillation of the beam size in a short channel. A simple understanding of this can be obtained by using the simple infinite parabolic density profile model of the plasma channel introduced earlier. It can be shown analytically [38] (under the paraxial approximation and for azimuthal symmetry, i.e., $m = 0$) that a Gaussian beam in-

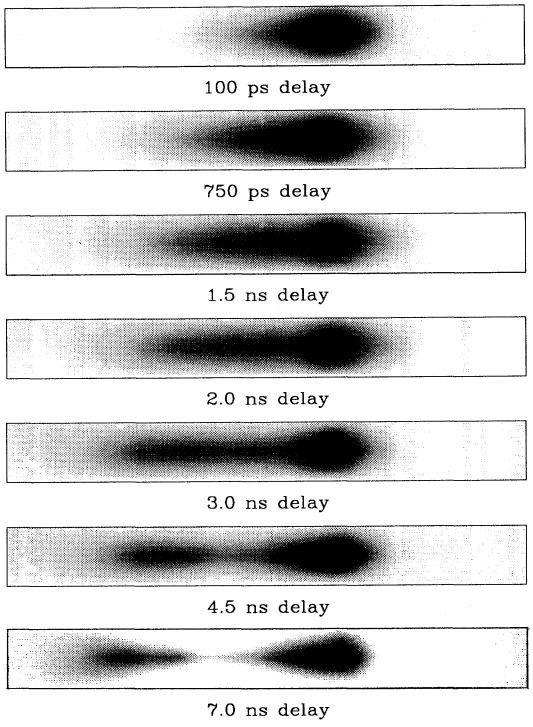

FIG. 5. Spark recombination emission (fluorescence) images for different delays between pump and probe pulses. The background pressure is 60-Torr N_2, pulse energies $E_1 = E_2 = 70$ mJ, spot size $w_0 = 10$ μm, and $\tau_p = 100$ ps.

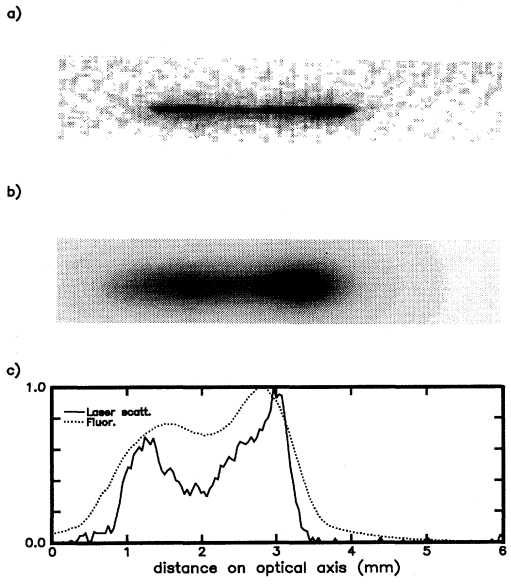

FIG. 6. Spark images for xenon at 30 Torr, with pulse energies $E_1 = E_2 = 70$ mJ. (a) Scattered laser light image collected with 3-nm bandpass filter centered at 1.064 μm. (b) Fluorescence image collected using a blue-pass filter (400–450 nm). (c) Lineouts of (a) and (b).

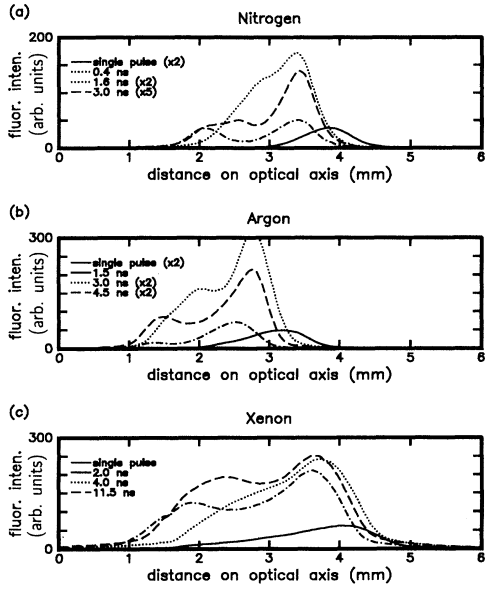

FIG. 7. Lineouts of fluorescence images collected for different gases (30 Torr, $E_1 = E_2 = 70$ mJ): (a) N_2; (b) argon; and (c) xenon. Laser is incident from the right. The single-pulse focal position is shifted toward the lens because of slightly different divergence under single-pulse conditions.

jected into a waveguide with such a profile oscillates in size if it does not match the fundamental mode. The oscillation period is $z_p = \pi a$, and depends on the channel curvature parameter a, not on the initial beam size or divergence. In the experimental conditions described above, the first pulse creates a plasma of length L_{ch} centered on the focal plane of the lens. Thus the second pulse, focused through the same lens, converges as it enters the plasma channel. A second focus and a second spark beyond the channel requires the beam to converge as it leaves the channel. The maximum peak separation corresponds to a curvature parameter a such that $L_{ch} \approx z_p$, in which case the exiting beam converges just as it entered. This is illustrated in Fig. 8, where $w(z)$ and the intensity $I(z)$ are plotted using the solution for propagation within the parabolic channel and free propagation outside the channel. As the curvature relaxes, the second focus moves away from the first, and finally disappears.

Effective channel curvatures (a) and lengths (L_{ch}) can be estimated by varying L_{ch} and a together (through $L_{ch} = \pi a$) to find the values that result in the measured maximum peak separation z_{max} (see Fig. 8). This result is not strongly dependent on the input spot size w_0 since the oscillation period z_p is independent of w_0. Assuming the position of the vacuum focus of the beam ($w_0 = 10$ μm) to be at the center of the channel gives an estimate for the maximum beam size w_{max} within the channel which is a lower limit for the channel width. The density difference $\Delta N_e(w_{max})$ at this radius is estimated using the calculated values of a. Table I lists the measured values of z_{max} and the spark length L_{spk}, along with the calculated values of L_{ch}, a, w_{max}, and $\Delta N_e(w_{max})$ for the data shown in Fig. 7. The values of L_{ch} are consistent with the measured single-pulse spark lengths L_{spk} for xenon and argon (measured as the FWHM of the fluorescence signal). For nitrogen, although $L_{ch} > L_{spk}$, it can be seen from Fig. 7(a) that it does lie within the region of fluoresence. At pressures higher than 30 Torr (for example, the 60-Torr data of Fig. 5), nitrogen fluoresence shows the structure of the second spark, while for the two noble gases the two peaks are not resolved. Thus it appears that the discrepancy between L_{ch} and L_{spk} for nitrogen is explained by reduced plasma emission for N_2 as compared with Xe or Ar for comparable target gas densities.

A computer code has been developed [33] to calculate the beam propagation for arbitrary channels numerically, using the method of Feit and Fleck [39]. Using this code to simulate the above experiment [37] shows that the beam still forms a second focus at a position close to that given by the infinite parabolic channel model, but there is some leakage or tunneling of the wave energy through the channel wall, especially when the maximum beam size within the channel approaches the shock front radius

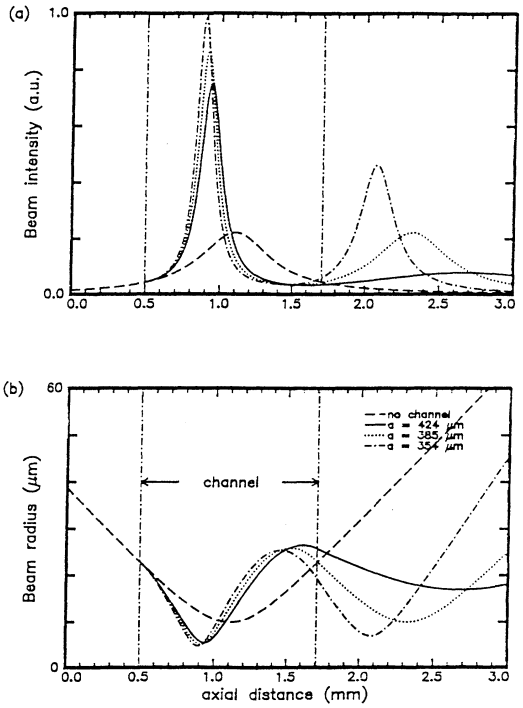

FIG. 8. Calculation of the intensity (a) and spot size (b) of a Gaussian beam propagating through a short channel with an infinite parabolic plasma density profile. The beam is incident from the left. The input beam has a vacuum spot size $w_0 = 10$ μm. The channel length here ($L_{ch} = 1.21$ mm) and the curvature ($a = 385$ μm) are chosen to match the peak separation in nitrogen (Table I).

TABLE I. Measured values (z_{max} and L_{spk}) and calculated values (L_{ch}, a, w_{max}, and ΔN_e) from the parabolic density profile model applied to the data of Fig. 7. The parameters are defined in the text.

gas	z_{max} (mm) (measured)	L_{ch} (mm)	L_{spk} (mm) FWHM (measured)	a (μm)	w_{max} (μm)	$\Delta N_e(w_{max})$ (cm^{-3})
N_2	1.38	1.21	0.80	385	26	4.5×10^{18}
Ar	1.26	1.12	1.10	357	25	4.9×10^{18}
Xe	1.72	1.49	1.55	474	31	4.2×10^{18}

(i.e., $w_{max}\approx r_m$). The propagation code also confirms that if the channel profile is not parabolic, an aberrated secondary focus occurs. This second focus is most distinct when the density cutoff allows only low-order modes to propagate. The calculated position of the secondary focus was found to be approximately the same as in the parabolic case if the density difference measured at the turning point of the beam $\Delta N_e(w_{max})$ is the same in both cases.

On-axis probe pulse far-field patterns (CCD_2, 40 shot averages) at various delays τ_d are shown in Fig. 9 for argon at 30 Torr with $E_1=70$ mJ and $E_2=10$ mJ. Increasing E_2 to 70 mJ did not qualitatively change the resulting images. The patterns at early delays indicate the presence of sharp spatial structure in the focus, consistent with scattering from a shock wave. A characteristic delay time τ_{d0} can be identified in these images. At short delay $\tau_d<\tau_{d0}$, large-angle scattering is present; at $\tau_d\approx\tau_{d0}$ the large-angle scattering disappears, while there is still modulation close to beam center; at long delay, $\tau_d>\tau_{d0}$, the beam profile modulation disappears. The times τ_{d0} are longer for the heavier gases and correspond to the characteristic times for spark lengthening discussed above. This correspondence implies that for $\tau_d<\tau_{d0}$, a second focus outside the main spark does not form since the shock wave is within the focal region of the probe pulse and most of the pulse energy does not fit inside the developing channel. Instead, the beam is scattered by the shock wave. At $\tau_d\approx\tau_{d0}$ most of the beam enters the channel, allowing the formation of the second focus, but enough of the beam energy is still scattered by the shock that there is still modulation of the far-field beam profile. For delay positions $\tau_d>\tau_{d0}$, the shock wave has moved radially out of the focal region, so most of the pulse energy passes through the radially increasing central profile and is lensed to cause the second spark.

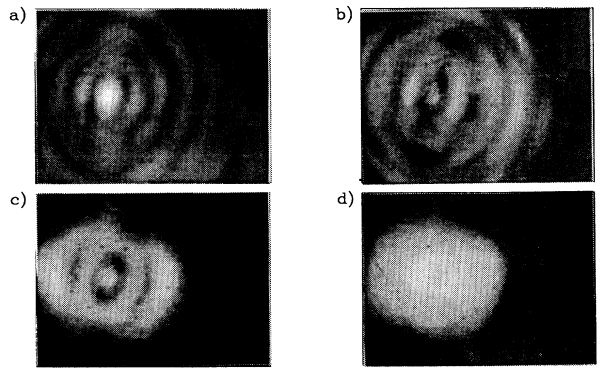

FIG. 9. Axial scattering images of probe pulse. Gas: 30-Torr Ar. Pulse energies: $E_1=70$ mJ and $E_2=10$ mJ. Probe pulse delays: (a) 0.2 ns, (b) 1.1 ns, (c) 2.9 ns, and (d) 5.9 ns.

The beam propagation code can be used to simulate the effects of the plasma on the transverse profile of the probe beam. The field is propagated to the end of the channel, where $E=E_{exit}(r)$. Since the beam after that point propagates in free space, a Fourier transform of $E_{exit}(r)$ gives the resulting field $E_{far\text{-}field}(\rho)$ in the plane of observation, where ρ is the radial position in the far field. Figure 10(a) shows calculations for a probe beam incident on a short column of plasma, with a peak in the plasma density on axis. This simulates probing at early delays of the plasma column formed by the first laser pulse. The converging beam is refracted away from the column, with the greatest refraction occurring near the center of the beam. If the index gradients are not too large, the resulting far-field pattern [Fig. 10(b)] shows an enhancement in intensity near the center. Now consider later delays, where a depression in the plasma density has formed along the optical axis due to formation of the shock wave [Figs. 10(c) and 10(d)]. For a range of shock radial positions, the central portion of the beam enters the channel, while the wings are refracted by the shock, away from the optical axis. After leaving the plasma region, the channeled and unchanneled portions of the beam interfere, creating a ring pattern in the far field [Fig. 10(d)]. This compares qualitatively to the images of Fig. 9. The greater the phase difference between the channeled and unchanneled parts of the beam (where this phase difference is proportional to the average plasma density difference between the beam center and wings), the smaller the ring spacing. Sharper refractive index gradients (i.e., due to the shock) result in a larger angular extent of the rings. As the shock front moves out of the focus, more of the beam energy enters the central region and is refracted without strong distortion of the beam profile. When the beam undergoes one oscillation in the channel, it exits the channel as it entered. The second focal spot

size is then roughly the same as the vacuum spot size, and the beam size measured at the chamber exit is close to the unperturbed beam size, as seen in Fig. 9.

These experiments demonstrated that a plasma shock wave initiated by an intense laser pulse could create a channel appropriate for guiding a second beam. It was clear from these data that longer guiding distances could be achieved by using longer plasma channels.

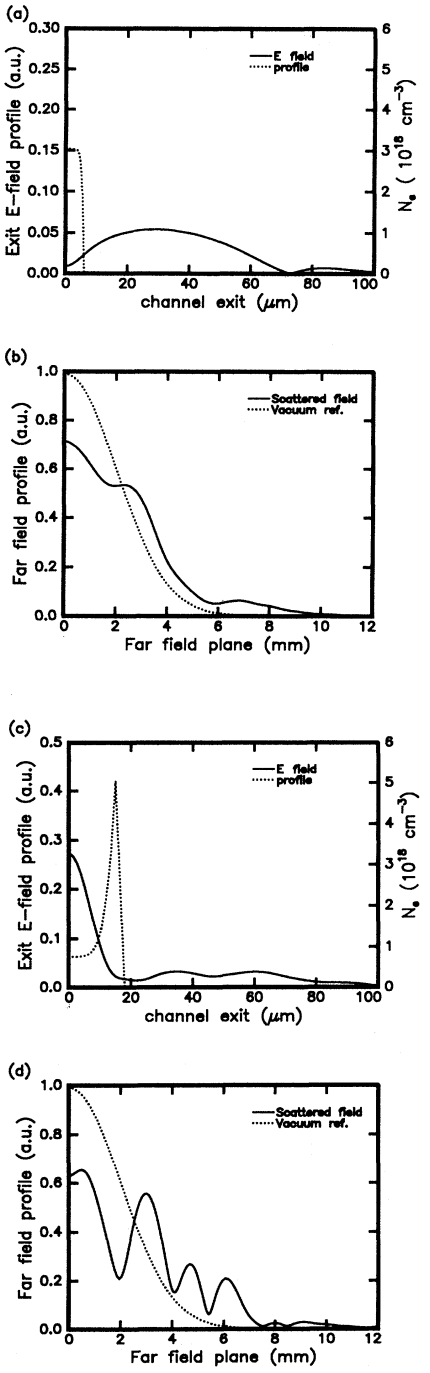

FIG. 10. Beam propagation calculation of the field distribution at the end of the short channel (1.2 mm) and the far-field distribution for [(a) and (b)] a plasma column which has no central minimum, which results in reflection away from the optical axis, and [(c) and (d)] a plasma column with a central minimum, which allows the central part of the beam to enter.

V. LONG CHANNEL EXPERIMENTS

A. Axicons

An axicon [14], an optical element that forms a line focus along its axis of revolution, was used to produce a longer channel. The axicon is more efficient than a cylindrical lens in concentrating light in a line focus, and produces a circularly symmetric focal region. The form of axicon used here was a polished glass cone. When a plane wave enters the planar side and emerges from the conical surface, it is converted into a conical wave front converging on the optical axis. For an input ray normal to the plane face of a conical transmission axicon with base angle α, the angle of approach γ to the optical axis is found from $n\sin\alpha=\sin(\alpha+\gamma)$, where α must be less than $\sin^{-1}(1/n)$, the critical angle. The rays at the input radial position ρ are related to those converging at the axial distance z by

$$z(\rho)=\rho c_\alpha=\rho\left[\frac{1}{\tan\gamma}-\tan\alpha\right] \tag{6}$$

where $z=0$ is at the axicon tip. When the beam does not fill the axicon aperture, the maximum length of the focal region is $z_{\max}\approx c_\alpha\rho_0$, which varies with the input beam radius ρ_0 and the base angle α. For a beam with $\rho_0=0.5$ cm entering an axicon with $\alpha=35°$, $\gamma=24.8°$, $c_\alpha=1.46$, and $z_{\max}=0.75$ cm.

A standing wave pattern near the optical axis results from the interference of the conical wave front with itself. For a collimated input beam $E_{\rm in}(\rho)$ polarized in the x direction, a calculation of the field near the optical axis using the Kirchoff diffraction integral and the method of stationary phase gives

$$E_x(r,z)=\left[\frac{\pi k\sin\gamma}{2}\frac{z}{c_\alpha}\right]^{1/2}E_{\rm in}(z)\times\left[\frac{1+\cos\gamma}{2}J_0(kr\sin\gamma)+\frac{1-\cos\gamma}{2}J_2(kr\sin\gamma)\right] \tag{7}$$

and

$$E_z(r,z)=\left[\frac{\pi k\sin\gamma}{2}\frac{z}{c_\alpha}\right]^{1/2}E_{\rm in}(z)[\sin\gamma J_1(kr\sin\gamma)]\ , \tag{8}$$

where k is the laser wave number, and Eq. (6) is used to map the input beam profile to the z axis. The small z component of the field (which vanishes at $r=0$) originates from input rays near the x-z plane. These rays develop a small axial component of polarization as they are

refracted toward the optical axis. The field profile near the axis results from the interference of rays refracted from opposite sides of the axicon, and is dominated by the $J_0(kr\sin\gamma)$ term in Eq. (7), since γ is usually small. The central spot size is $r_0=x_0/(k\sin\gamma)$, where $x_0\approx 2.405$ is the first zero of $J_0(x)$. Since γ is constant, the interference pattern, and therefore the spot size, is invariant for $z<z_{\max}$ along the optical axis. For a nonconical axicon, or a nonparallel input, the angle γ and the spot size depend on z. The intensity profile along z can therefore be modified by adjusting the input beam divergence [40,41] or the axicon surface of revolution [42].

The variation of the amplitude along the optical axis is also determined by the input beam profile

$$I(z)=\frac{\pi k\sin\gamma}{2}\frac{z}{c_\alpha}I_{\rm in}(\rho(z))\frac{(1+\cos\gamma)^2}{4}\ , \tag{9}$$

where the angular factor at the end results from the projection of the polarization along the optical axis. A flat input beam profile would yield an axial intensity profile that linearly increases until the cutoff at the edge of the axicon. The peak intensity along the optical axis occurs at $z=\xi z_{\max}$, with ξ a constant determined by the input beam profile ($\xi=\frac{1}{2}$ for a Gaussian input beam). Since the peak intensity follows $I_{\max}\propto\xi z_{\max}P_{\rm in}/\rho_0^2\propto P_{\rm in}/z_{\max}$, where $P_{\rm in}$ is the input power, the intensity is inversely proportional to the length of the focal region. As an example, a 100-mJ, 100-ps pulse, directed to an axicon ($\alpha=35°$) in a beam radius of $\rho_0=0.8$ cm, reaches a peak intensity equal to the saturation intensity for single ionization of xenon [43] $I_{\rm sat}\approx 1.2\times 10^{13}$ W/cm^2.

As a comparison, consider the use of a cylindrical lens to form the plasma channel. The focal region of a cylindrical lens does not have circular symmetry, with a focal aspect ratio of $2z_0/d$, where z_0 is the Rayleigh length of the focal line of width d. To produce $I\approx 1.2\times 10^{13}$ W/cm^2, for $\lambda=1$ μm, focal line length $D=1$ cm, and $d\approx 4$ μm (aspect ratio ~ 6), requires $P_{\rm in}\approx 5$ GW (0.4 J in 100 ps), four times as much as with the above axicon.

For most of the experiments described here, an axicon with base angle $\alpha=35°$ was used, producing a spark about 0.8 cm long. A spark over 2 cm long has been produced using an axicon with $\alpha=20°$, but since the focused intensity was close to the ionization threshold, slight variations in the pulse energy led to changes in the length of the spark. For the $\alpha=35°$ axicon, a lineout of a magnified image of a cross section of the focal region (recorded with a CCD camera and a 60× microscope objective) is shown in Fig. 11. The calculated spot size is $2r_0\approx 2$ μm, and the measured FWHM of the spot is 3 μm, limited in part by the camera resolution. For the xenon-seeded breakdowns used in the current experiments (with $\alpha=35°$), the energy required for a uniform breakdown in the axicon focus is roughly 150 mJ per cm of spark. A mix of $\lambda=0.532$- and 1.064-μm light decreases this energy requirement (due to the greater initial fraction of electrons produced by multiphoton ionization). Axicon sparks have been generated previously in the avalanche breakdown regime at pressures ranging from 0.02 atm [44] to several atm [45], using long pulses

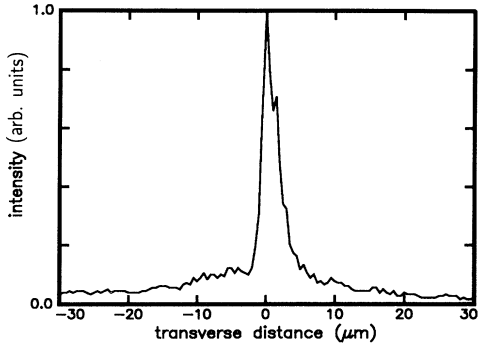

FIG. 11. Measurement of the axicon focal spot, using a 60× microscope objective and a CCD with 30-μm pixel spacing. The HWHM is approximately 1.5 μm.

(5–40 ns) and high pulse energies (up to 100 J). A periodic structure in the breakdown spark has been observed to develop within the first few nanoseconds of the breakdown [46], in which filaments were seen to form along the direction of the rays approaching the optical axis. The structure has been attributed to self-focusing in the gas or plasma [47]. The sparks generated in the present experiments, with 100-ps pulses and lower pressure (30–200 Torr), are free of such structure, most likely because little radial plasma motion out of the high intensity region occurs during the pulse.

Due to the difficulty in polishing the conical surface to the same degree of quality as found routinely in spherical and planar optical surfaces, it would be expected that imperfections in the surface figure would lead to small-scale variations in the axial intensity profile. Here, however, the laser pulse duration is sufficiently long that there is inverse bremsstrahlung heating during the pulse. Thermal conduction along the length of the spark during and shortly after the pulse leads to an axial temperature profile more evenly distributed than the intensity profile. Subsequent collisional ionization then smooths any initial nonuniformity in the plasma. Using the thermal conductivity scaling from above (Sec. II B), the thermal diffusion lengths on time scales of 1 ps, 100 ps and 1 ns are approximately 20, 200, and 700 μm, respectively, at $T_e=50$ eV. Generation of a uniform spark may be difficult with subpicosecond pulses because of insufficient heating and thermal conduction during the pulse (Sec. II B).

B. Experimental arrangement

The 170–200-mJ output of the Nd:YAG regenerative amplifier system was split into two paths with a polarizer (P_1), with one beam producing the axicon spark and the other to be guided by the channel (see Fig. 12). The latter beam passed through a corner cube mounted on a variable delay line (12-ns range) and a beam expander before focused with the coupling lens (L, 250-mm focal length) through the chamber window. A quarter-wave plate (QWP) was required to relinearize the polarization after the internal reflections in the corner cube. A half-wave plate (HWP_2) and polarizer (P_2) were used for lens beam

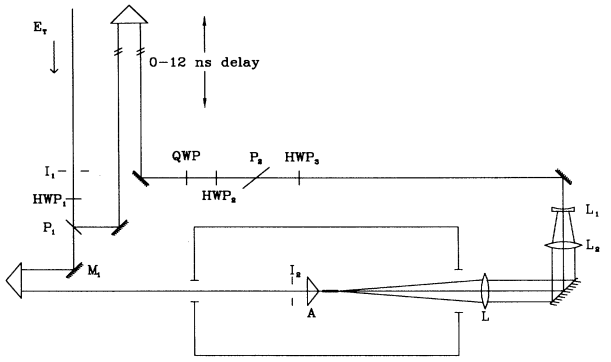

FIG. 12. Long channel experiment.

intensity adjustment, and the final half-wave plate (HWP_3) controlled the polarization of the coupling beam. Normally S polarization was preferred for side observations of Thomson scattering. The focal spot size was measured by imaging the spot with a microscope onto a CCD camera, and was 10–15 μm ($1/e^2$ radius), depending on the input beam size. The coupling adjustment was made outside the vacuum chamber through three-axis precision adjusters on the focusing lens. This technique for moving the focal position slightly affected the angle of approach to the channel, but careful prealignment of the beam ensured that the angle was very small (less than 0.2 mrad). An axial hole in the axicon of diameter $2a=0.125$ in. allowed transmission of the counterpropagating coupling lens beam. The hole resulted in only a small reduction in spark length, due to the small radial weighting factor in the region close to the axicon apex [see Eq. (9)]. The length of the spark was controlled with an iris (I_2) near the entrance face of the axicon.

Side-scattered laser light and recombination emission were imaged onto a cooled CCD camera (CCD_1; see Fig. 13) as in the experiment described in Sec. IV. The light

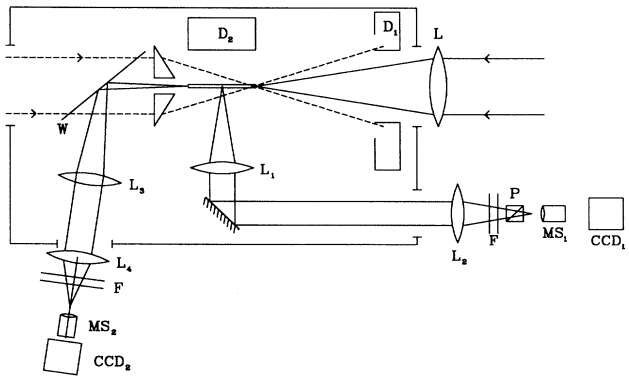

FIG. 13. Optical diagnostics for long channel experiments. D_1 is a dump for the axicon beam, and D_2 is a light trap to form a dark background for observations through lens L_1. The size of the hole in the axicon is exaggerated to show the rays more clearly.

scattered or emitted at 90° to the optical axis was collected and reimaged outside the chamber with lenses L_1 and L_2. CCD_1 either collected this image directly or was placed at the image plane of a microscope objective (MS_1). A polarizer (P) in the imaging path was used to select either scattered light from the coupling lens beam or the axicon beam. Note that although the observation direction was nominally along the polarization direction of the axicon beam, the small component of the field along the optical axis [for $r\neq 0$, see Eq. (8)] allowed some axicon light scattered from the plasma to be observed. A cooled CCD camera was used for these measurements, allowing integration of the signal over many shots at the laser repetition rate of 10 Hz. The long integration times (typically 1500 shots) made it imperative to reduce any stray light and background signal. Most of the background signal was subtracted in the computer by blocking the coupling lens beam and collecting a reference image. This reference image contained residual scattered and stray light from the axicon beam, camera dark current and amplifier offset, as well as any plasma emission falling within the bandpass of the interference filter.

The intensity distribution of the beam exiting the plasma channel was measured by relaying an image of the channel exit to camera CCD_2 (see Fig. 13). A Brewster window (W) placed before the axicon reflected some of the S-polarized lens beam, while the P-polarized axicon beam was transmitted through the window with minimal losses. Collimation lens L_3 was placed with the exit of the channel (nearest the axicon) at its focus. The light emerging from the channel was imaged by lens L_4 to a point outside the chamber. This spot was then magnified by a microscope objective (MS_2) and imaged onto CCD_2. Two image planes were of interest, those corresponding to the entrance and exit of the waveguide. MS_2 and CCD_2 were mounted on an adjustable rail so that either image plane could be viewed. These two planes were distinct, since the channel lengths were much longer than the Rayleigh length of the coupling beam focus (always greater than a factor of 20). These images of the coupling lens focus and the channel exit were viewed in real time (at 10 Hz) to very and optimize the coupling into the channel. For example, when the lens beam did not pass through the axicon plasma, an undistorted focal image of the entrance plane of the channel was observed. When some portion of the beam passed through the axicon plasma, the image became distorted as the light was either coupled into or scattered by the channel. After centering this image, the microscope objective was moved back to find the image plane of the channel exit, where the channeled beam appeared as a small spot.

C. Plasma channel guiding

Images and lineouts of side-scattered laser light are shown in Fig. 14 for a mix of 30-Torr Xe and 95-Torr N_2, axicon pulse energy $E_1=160$ mJ (estimated peak line focus intensity 2×10^{13} W/cm^2) and lens pulse energy $E_2=15$ mJ. As discussed in Sec. III B, multiphoton ionization of the xenon provides the seed electrons to promote avalanche ionization of the nitrogen. Here the full

length of the long spark region was imaged onto CCD_1. Figure 14(a) shows the light scattered from the axicon pulse alone. The channeled light alone (with the cube polarizer blocking the axicon light) is shown in Fig. 14(b) for a delay $\tau_d = 6$ ns (100-shot average). A bright scattering peak is seen at the entrance to the channel, followed by weaker scattering from the plasma center, and another strong scattering peak at the channel exit. Above a threshold of about 5 mJ, the channel entrance and exit scattering peaks were observed to increase nonlinearly with the intensity of the coupling lens pulse. The heights of the two peaks indicate that the light fluxes incident at the scattering points were comparable. The mechanism for the enhanced scattering at the ends will be discussed in Sec. V G. The second peak disappeared if the coupling lens focus was detuned to the side by less than 15 μm. Blocking the axicon beam eliminated all but a breakdown peak at the lens focus. The guiding distance here is 7 mm, 24 times the Rayleigh length of the 10-μm focal spot.

Figure 15(a) is an image of the channeled beam at the waveguide exit, for a mix of 30-Torr Xe and 170-Torr N_2, $E_1 = 100$ mJ and $E_2 = 25$ mJ (30-shot average). The lineout data from this image (points) and a fit of these data to a Gaussian profile (solid line, with a $1/e^2$ radius of 25 μm) are shown in Fig. 15(b). By contrast, the unguided beam, focused at the channel entrance (dashed line, taken with the axicon beam blocked), has a $1/e^2$ radius of about 240 μm at the channel exit plane. The beam exiting the channel was stable in position and intensity over many shots, indicating that the propagation is not sensitive to small changes in intensity. The stability of the output beam depends primarily on the stability of the axicon plasma, which in turn depends on how close the axicon focal intensity is to the ionization threshold. If the intensity is very close to the threshold, the effective length of the channel fluctuates with laser energy. The 2.2-cm spark generated with the $\alpha = 20°$ axicon was seen to guide a pulse for over 70 Rayleigh lengths, though not for every shot due to the spark length fluctuations. As a check on the confinement of the beam, the exit mode was imaged for different axicon spark lengths. An iris (I_2), placed at the entrance to the axicon, limited the radius of the input beam, controlling the length of the channel [see Eq. (9)]. Figure 16(a) shows lineouts of two fluorescence images for an open iris and an iris set to 14-mm diameter, which shortened the plasma length by 1.5 mm. The lineouts of the resulting exit modes [Fig. 16(b)] show that the beam size is constant to within 15%, demonstrating that the beam is channeled at a small size throughout the guide.

The channel widening with delay is verified in Fig. 17, under the same conditions of Fig. 14. Magnified laser

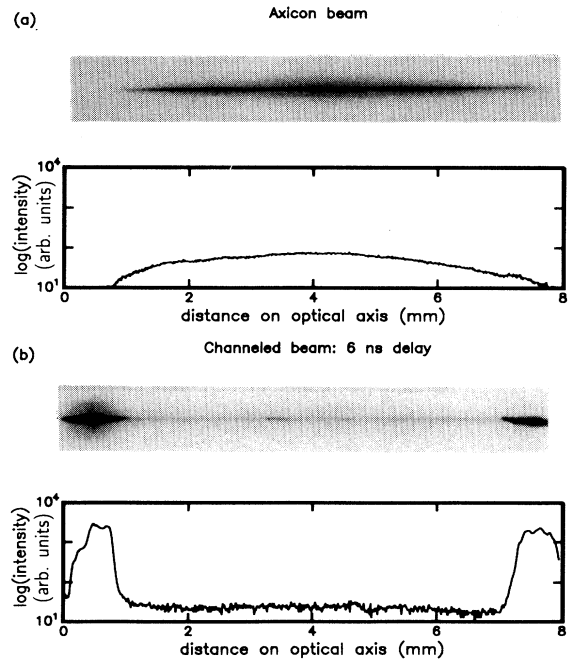

FIG. 14. Images and axial lineouts of scattered laser light from the axicon focal region. Gas: 30-Torr Xe–95-Torr N_2. Pulse energies: $E_1 = 160$ mJ and $E_2 = 15$ mJ. (a) Axicon beam alone. (b) Channeled beam injected after a 6-ns delay. The background is subtracted from each.

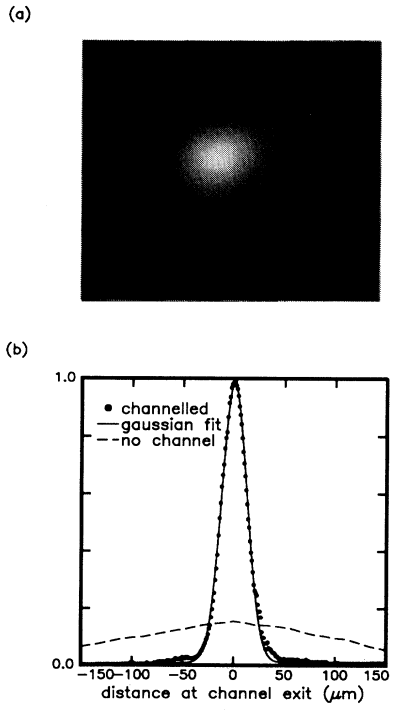

FIG. 15. (a) Mode profile at channel exit. The beam is focused at the entrance of the channel and couples to low-order channel mode(s). Gas: 30-Torr Xe–170-Torr N_2; pulse energies: $E_1 = 100$ mJ and $E_2 = 25$ mJ; delay: 12 ns. (b) Lineout of this image, where the least squares fit to a Gaussian gives a FWHM of 25 μm. The dashed line shows the size of the beam at this focal plane when the axicon spark is not present.

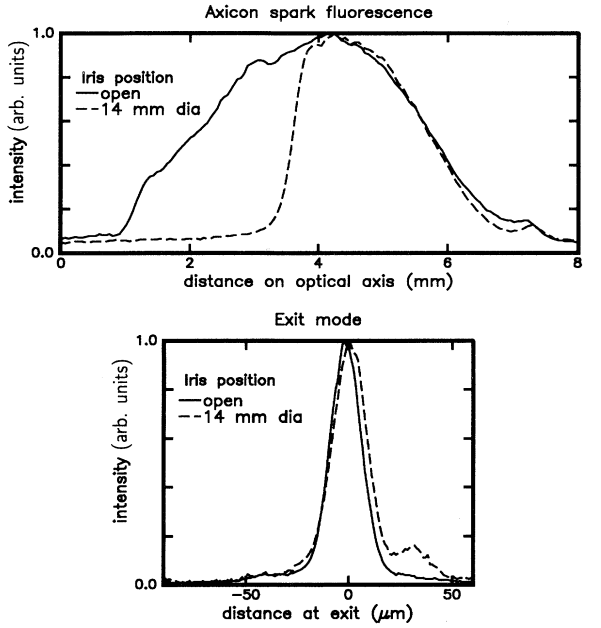

FIG. 16. An iris at the entrance to the axicon is used to control the beam size entering the axicon, thereby controlling the channel length. Gas: 30-Torr Xe–170-Torr N_2. Pulse energies: $E_1=160$ mJ and $E_2=25$ mJ. (a) The lineout of the fluorescence from the spark shows a 1.5-mm spark length reduction, with the iris closed to a 14-mm diameter. (b) Exit mode lineouts. The exit mode sizes are comparable: 18 μm for the shorter channel and 16 μm for the longer channel.

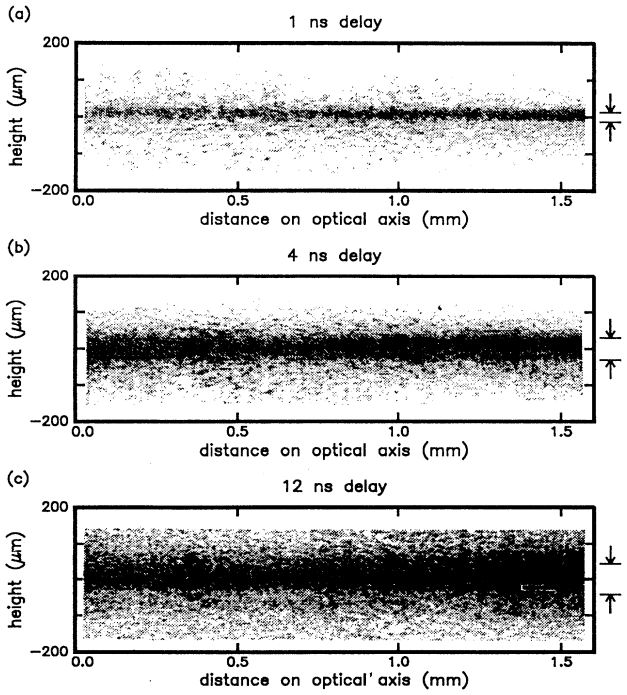

FIG. 17. Side images of laser scattering from middle section of channel. Gas: 30-Torr Xe–95-Torr N_2. Pulse energies: $E_1=160$ mJ and $E_2=15$ mJ. Widths marked with arrows are (a) 26, (b) 60, and (c) 86 μm.

scattering images of the center region of the channel (using microscope objective MS_1 and cooled camera CCD_1) are shown for delays of 1, 4, and 12 ns, where the widths are 26, 60, and 86 μm. These widths extend for the full length of the channel. The signals were integrated over 1500 shots, and the background signal was subtracted as outlined above.

At lower chamber pressures, the CCD cameras were not adequately sensitive to measure the Thomson scattered light. Figure 18 shows a sequence of axial lineouts of fluorescence emission collected with CCD_1 (30 Torr of Xe, $E_1=145$ mJ, $E_2=40$ mJ, and $\tau_d=15$ ns). These images were taken with blue-pass and IR-blocking filters. This figure shows that there is a center position of the coupling lens that gives the most uniform increase in spark emission along the whole length and the lowest emission at the channel entrance. This position also gives the greatest degree of coupling into the output mode as measured with CCD_2. When the lens was translated by 15 μm to any transverse position, the emission was

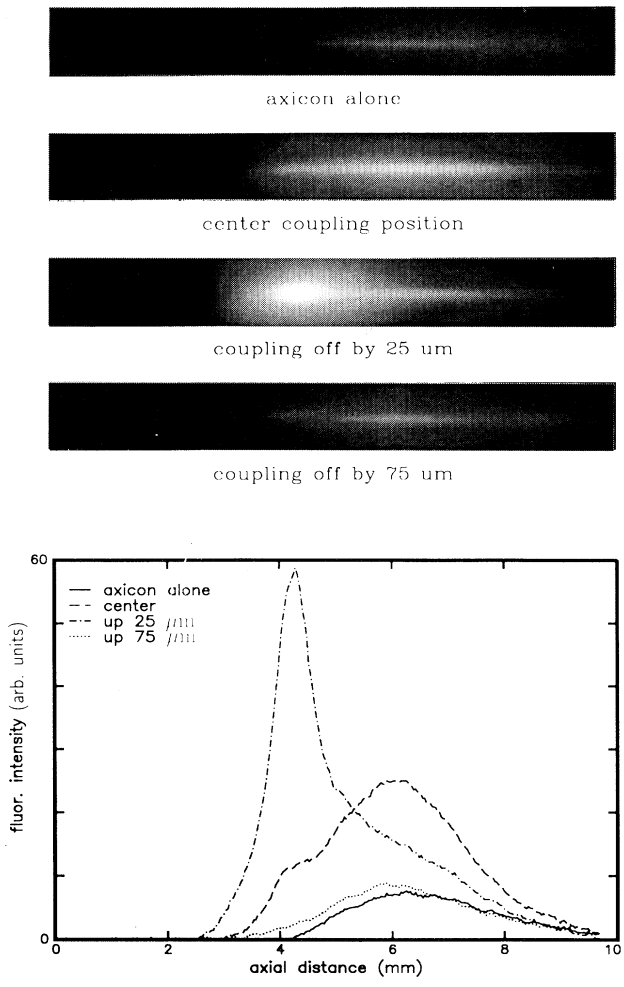

FIG. 18. Images and lineouts of fluorescence from the axicon focal region as input coupling is detuned. Gas: 30-Torr Xe. Pulse energies: $E_1=145$ mJ and $E_2=40$ mJ. Delay: 15 ns.

enhanced at the entrance to the axicon plasma, while the emission along the length decreased. Translating the coupling lens by an additional 20 μm caused the emission to decrease to the same level as that due to the axicon alone. The enhancement in the fluorescence at the spark tip results from the interaction of the lens beam focus with the higher density plasma of the expanding shock. As the delay was increased, so was the transverse displacement of the coupling lens required to maximize the brightness at the spark entrance. This is consistent with the presence of a radially expanding shock front.

D. High density multimode propagation

It is clear from Eq. (5) that a larger density difference and/or channel size allows higher order modes to propagate. For sufficiently high chamber pressures, the total density difference (to the peak of the shock) can be substantially higher than the minimum needed to guide a beam, especially since inverse bremsstrahlung heating and resulting collisional ionization, both of which increase with density, lead to multiple ionization. Increased laser heating also drives the expansion at a greater rate (since the initial shock speed is approximately the ion acoustic speed c_s), leading to larger channel diameters for a given delay compared to the lower density case.

If the waveguide supports multiple modes, the propagation of the channeled light depends on the coupling of the input beam to the modes. The input beam in Fig. 15 was focused near the channel entrance and coupled to a low-order mode. An input beam of a size comparable to the fundamental channel mode size may be coupled to higher-order modes if it diverges as it enters the channel. (An input beam smaller than the fundamental mode couples to higher-order modes even when it is collimated at the entrance.) When the input beam does not selectively couple into just a few low-order modes, the exiting beam is most often a mixture of many modes, without easily classifiable structure. Figure 19 shows multimode exit beam profiles for which the input focus was placed about 1 mm before the channel entrance, for several delays. At 8 ns, four lobes in the image indicate the presence of an $m=2$ mode, while at 10 and 12 ns an $m=1$ mode appears to dominate, and $p \geq 2$ at longer delays. A slight angular misalignment between the axicon spark center line and the direction of the coupling beam results in the azimuthal orientation of the lobes. At the longer delays, a well-defined boundary develops within which the modes are confined. This is the region in the channel wall where the field is exponentially damped. The radius of this boundary, r_s, increased with the delay of the channeled beam, moving from $r_s \approx 40$ μm to $r_s \approx 70$ μm over a span of 6 ns, giving an average speed $v_s \approx 5 \times 10^5$ cm/s.

As described earlier in Sec. IV, a Gaussian beam propagating in a quadratic profile waveguide will oscillate in size if the input beam does not couple to azimuthal modes and is either uncollimated or a different size from the fundamental mode. Here conclusive evidence was not seen for oscillations of the beam diameter within the channel. For a lowest-order mode spot size $w_0 \approx 10$ μm, the period of oscillation in a parabolic channel is $z_p = \pi a \approx 1$ mm and approximately seven oscillations

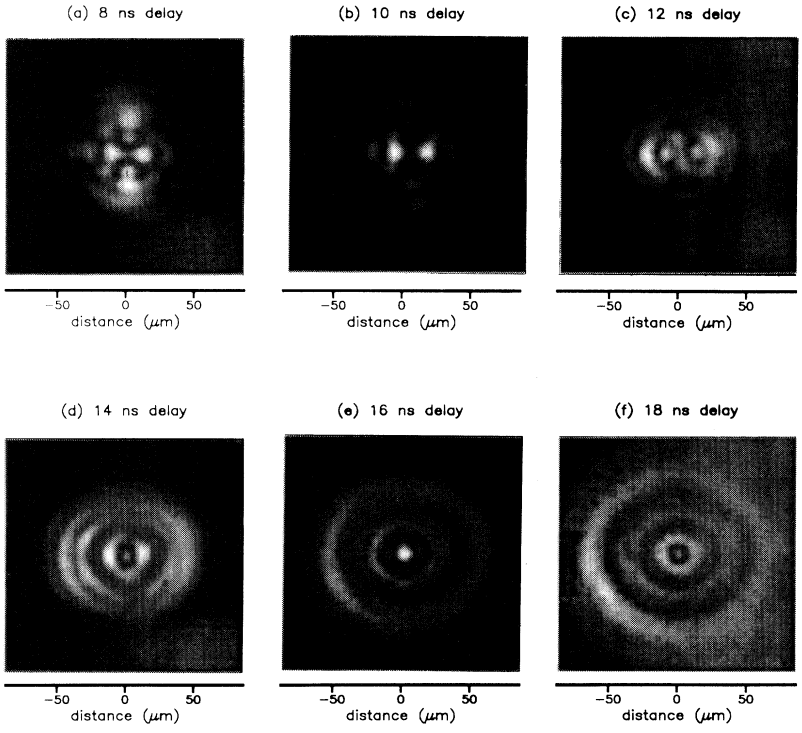

FIG. 19. Exit modes for various delays. The input beam was focused 1 mm in advance of the channel entrance, forcing it to couple to high order modes. Gas: 30-Torr Xe–170-Torr N_2. Pulse energies: $E_1 = 160$ mJ and $E_2 = 25$ mJ.

occur along the length of the channel. The transverse resolution of the imaging may have limited the capability to see such variations. However, it can be shown with the beam propagation code that a beam does not always oscillate periodically in an arbitrary density profile [37]. The beam profile in a waveguide containing only bound modes is the result of interference of these modes. For a parabolic channel, the phase difference between modes is an integer multiple of the period $z_p = \pi a$, and the resulting mode beating ensures that a Gaussian input will maintain its Gaussian shape as it oscillates in size. Nonparabolic channels, such as those predicted by the plasma dynamics code (see Fig. 1), do not have this relationship between the mode phases, so the propagation is aperiodic. An initially Gaussian beam that couples to many waveguide modes quickly loses its Gaussian character as the relative phases of the modes change.

E. Low density single-mode propagation

At background pressures below approximately 100 Torr, the maximum possible electron density difference is low enough that the beam is channeled only in low-order modes. The plasma dynamics code shows that at this pressure, field ionization dominates, followed by inverse bremmstrahlung heating of the electrons. At low background pressures, movement of the input beam transversely or axially does not change the exit mode shape, it only changes the degree of coupling. Figure 20 shows a sequence of output beam profiles as the coupling lens focus was moved along the optical axis away from the tip of the channel by 0.625-mm increments (30-Torr Xe, 40-Torr N_2, $E_1 = 160$ mJ, $E_2 = 15$ mJ, and $\tau_d = 10$ ns). The coupling decreases [Fig. 20(a)] as expected as the lens is moved back, but the normalized beam profiles [Fig. 20(b)] show that the mode shape remains constant, consistent with single-mode waveguide behavior. The least-squares fit to a Gaussian is very close to the data, with some small variation in the wings of the profile. One of the lineouts of Fig. 20(a), fit to a Gaussian, gives $w_{ch} = 17$ μm. Despite the good fit, it would be difficult to infer the details of the exact density profile from the measured mode shape, since the lowest order mode is very nearly Gaussian for a range of channel profiles [33]. The mode radius w_{ch} gives an estimate $\Delta N_e(w_{ch}) = 1/(r_0 \pi w_{ch}^2)$ for the density difference between $r = 0$ and $r = w_{ch}$; for Fig. 20, $\Delta N_e(w_{ch}) = 4 \times 10^{17}$ cm^{-3}. This value is only weakly dependent on the actual density profile. An upper density difference limit at $r = r_m$ can be found for a particular density curvature exponent α by noting that the $p = 0$, $m = 1$ mode is not bound. For a parabolic profile, Eq. (5) gives $\Delta N_e(r_m) < 4/(r_0 \pi r_m^2)$, where $\Delta N_e(r_m) = \Delta N_e(w_{ch}) \times (r_m / w_{ch})^2$, leading to $r_m^2 < 2w_{ch}^2$.

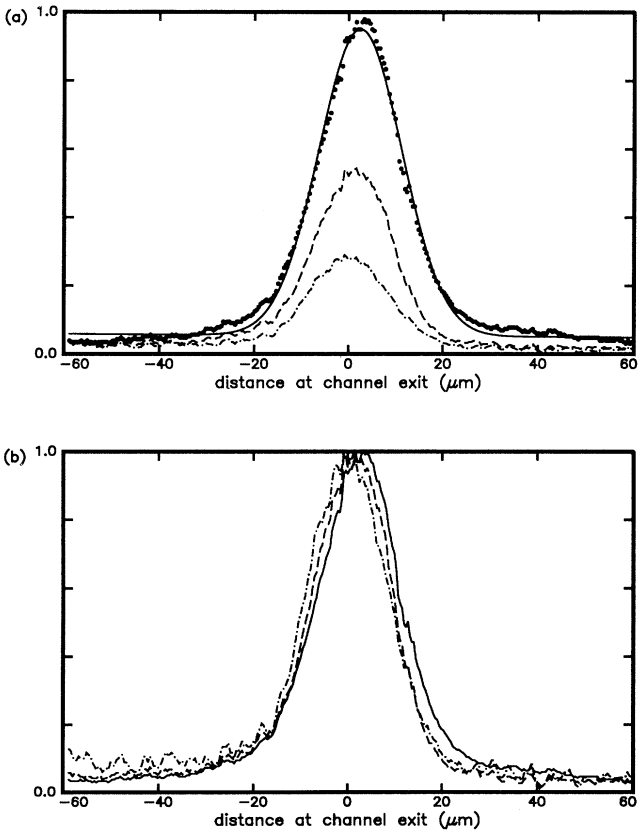

FIG. 20. Lineouts of exit mode profiles for a single-mode plasma waveguide as the coupling lens position is moved away from the channel entrance along the optical axis in 0.625-mm increments. (a) Coupling is strongest for the lens focus at the channel entrance, and decreases as the focal position is moved back. (b) Normalized plots of same data show that the mode shape remains constant. Gas: 30-Torr Xe–40-Torr N_2. $E_1 = 165$ mJ and $E_2 = 25$ mJ. Delay: 12 ns.

Figure 21 shows the variation of the measured exit mode radius with delay (30-Torr Xe, $E_1 = 165$ mJ, and $E_2 = 25$ mJ). At first, the mode size decreases with increasing delay. As the curvature of the plasma density profile relaxes during the plasma expansion, Eq. (3) predicts an increase in the mode size w_{ch}. Under the shortest delay conditions, Eq. (3) underestimates the density difference needed to guide the measured mode because the mode penetrates through the shock wall of the small radius channel. Figure 22 illustrates this with calculated

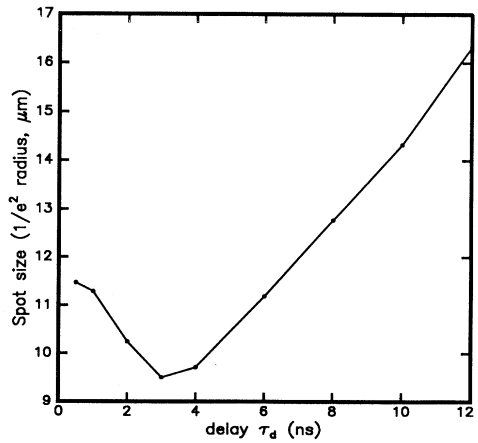

FIG. 21. Channeled mode spot size vs delay. Gas: 30-Torr Xe. $E_1 = 165$ mJ and $E_2 = 25$ mJ.

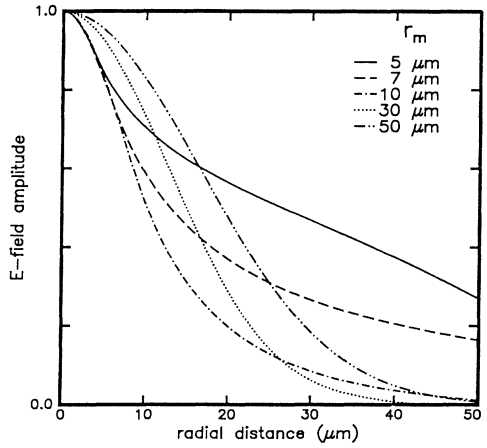

FIG. 22. Calculated fundamental mode profile for a quadratic channel with a constant plasma density outside the radius r_m. Each plot has the same maximum density difference as r_m is varied.

lowest order modes for channels with a constant electron density for $r > r_m$, each with the same $\Delta N_e(r_m)$. For wider channels (such that $w_{ch} < r_m$), the spot size increases with r_m as the curvature relaxes, and Eq. (3) predicts the correct spot size. For small channels ($r_m \leq w_{ch}$), the mode size increases with decreasing r_m, extending well beyond r_m as it approaches cutoff. Additionally, as will be illustrated in Sec. V F, small channels with decreasing electron density beyond r_m exhibit radiation tunneling through the cylindrical plasma shock wave at r_m, which contributes to the field at radial positions beyond the central mode peak.

F. Leaky mode propagation

As discussed in Sec. II C, the finite thickness of the channel wall can result in the leakage of propagating energy from the channel. Figure 23 shows a sequence of laser scattering images vs delay for the full length of the channel along with axial lineouts (on a log scale) for the same conditions as Fig. 14. At the shortest delay (1 ns), the scattered light signal decreases exponentially along the length of the channel, and there is no enhanced scattering at the exit. As the delay is increased (2 ns), enhanced scattering begins to appear at the channel exit, with the signal still attenuated along the channel. At 6 ns, the scattering is constant, indicating that the intensity of the channeled beam is approximately constant along the channel length. The enhanced scattering peaks at the entrance and exit are roughly equal in magnitude for this delay position. The lineout of the image taken at the longest delay ($\tau_d = 12$ ns) shows that the beam comes to a gradual focus close to the exit of the channel. Here the scattering at the exit was larger than at the entrance.

Figure 24 shows normalized images of the exit modes for all four delay positions. The energy throughput (measured by integrating the images) rises sharply over the delay range 1–4 ns, then levels off. This strong increase in throughput over the short delay range is consistent with the observations above of the decreasing leakage of the beam from the channel. The ratio of the scattered light

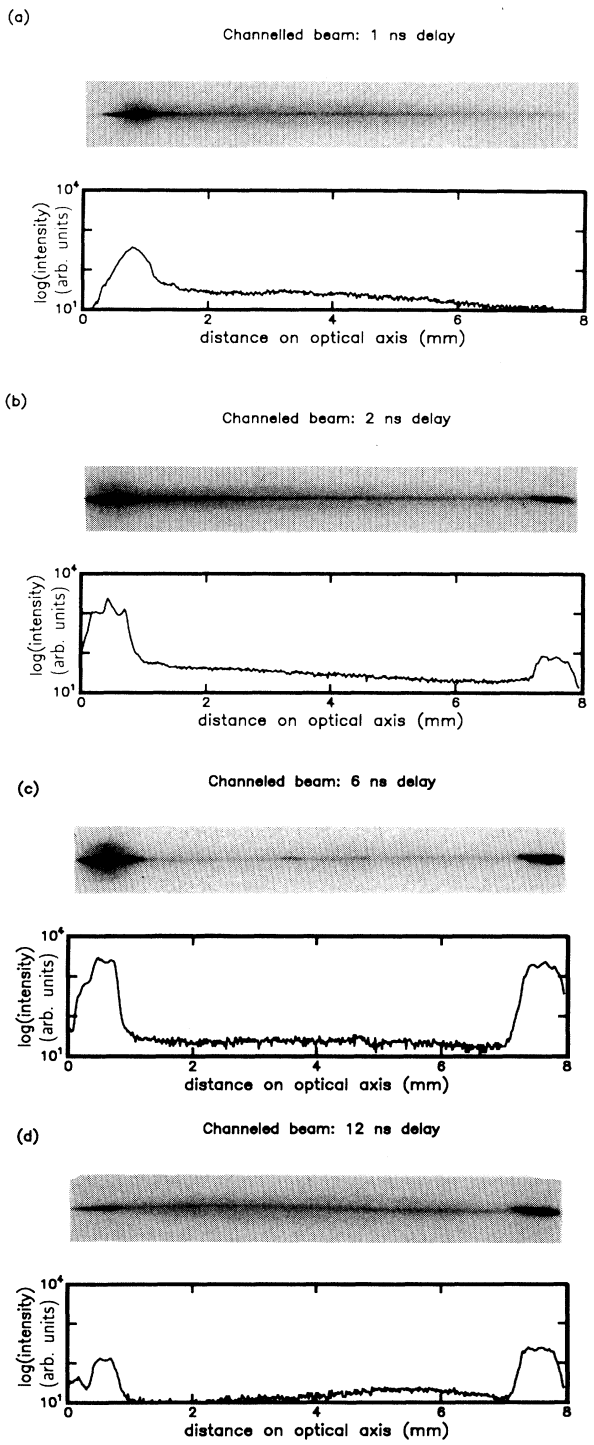

FIG. 23. Images and axial lineouts of scattered laser light, showing reduction in leaky mode attenuation at longer delay. Laser is incident from left. Gas: 30-Torr Xe–95-Torr N_2. Pulse energies: $E_1 = 160$ mJ and $E_2 = 15$ mJ.

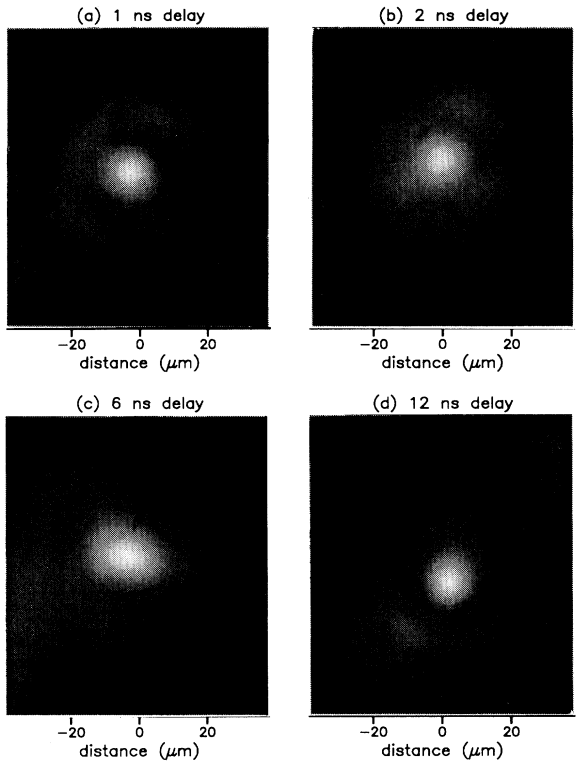

FIG. 24. Exit mode images for the data shown in Fig. 23. Relative throughput: (a) 0.21; (b) 0.33; (c) 0.82; and (d) 1.0.

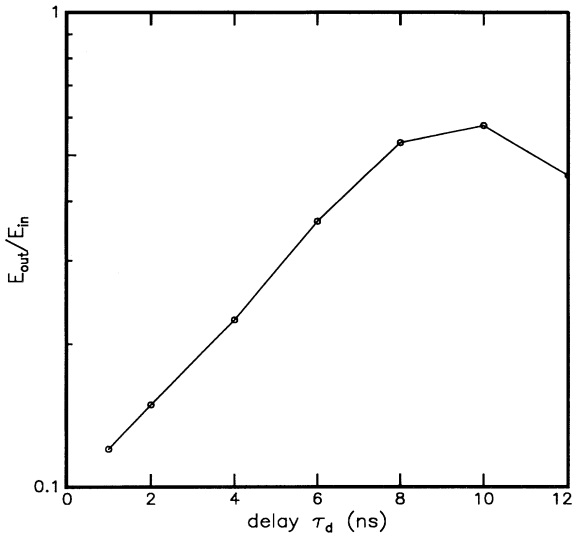

FIG. 25. Absolute energy throughput vs delay. Gas: 30-Torr Xe–60-Torr N_2. $E_1 = 165$ mJ and $E_2 = 25$ mJ. Spot size at the maximum energy throughput is 13 μm.

intensity near the exit to the intensity near the entrance (just inside the large scattering peaks) is 0.22 for the 1-ns delay position and 0.36 for the 2-ns delay. The throughputs for these two delay positions relative to the maximum delay position are 0.21 and 0.33, respectively, demonstrating that the side-scattered light is a good relative measure of the propagating intensity. The rings in the exit modes at 1 and 2 ns result from the leaky mode tunneling rather than from higher-order bound modes. The rings disappear at longer delays, in distinction to the behavior of a higher-order mode. The small size of the output mode at 12-ns delay is further indication of a secondary focus near the exit, consistent with the observations above the larger side scattering there. This reduced thoughput at short delays is also seen at lower densities. Figure 25 shows the measured throughput versus τ_d for a gas mixture of 30-Torr Xe and 60-Torr N_2. The throughput was measured as the fraction of the light in the lens focal spot that emerged from the channel exit. The measured peak thoughput under these conditions is close to 60% (in a spot size of 13 μm), giving a channeled peak intensity of approximately 10^{14} W/cm^2.

The attenuation of Figs. 23(a) and 23(b) is not attributable to inverse bremsstrahlung absorption, for which calculations show a bleaching effect as the guided pulse heats the channel (see Sec. V G below). The attenuation at the earliest delay positions is caused by strong leakage from the narrow channel. To illustrate this, Fig. 26 shows a beam propagation calculation for a channel profile generated by the plasma dynamics code at early delays. The input beam ($w_0 = 10$ μm) is focused at the entrance of a channel with $r_m = 8$ μm and decreasing density for larger radial positions. A central region of decreasing peak field is seen to propagate down the channel center, with tunneled radiation diverging at a slight angle to the channel axis, forming radial rings.

G. Coupling and attenuation

The factors which influence the energy throughput of the channel can be divided into two categories: input coupling efficiency (determined by mode matching and scattering at the entrance), and attenuation of the channeled beam (from absorption, side scattering or back-

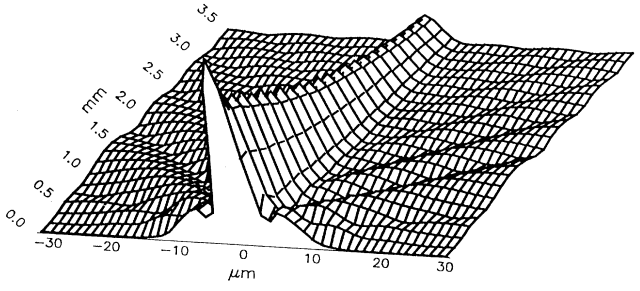

FIG. 26. Calculation of the beam propagation in a channel with a small channel radius and an electron density that peaks radially, then falls to zero, showing leakage or tunneling radiation. The radius to channel peak electron density is 8 μm, and the input spot size is 10 μm at the channel entrance.

scattering from the plasma channel, or waveguide leakage or tunneling). The energy throughput was determined by comparing an integration of the signal in the exit mode image with the same measurement made of the input focal spot (after positioning MS_2 to observe the focal plane of the coupling lens). This throughput ratio can be quite high: for example, in the data shown in Fig. 15, the channel throughput was 75%.

The origin of the enhanced laser scattering at the channel entrance and exit is Fresnel reflection of the beam from the axially propagating shock wave interface between the plasma and the surrounding gas. In previous work [48] enhanced scattering observed at 90° from a Nd:glass laser-produced spark in helium (at 1–4 atm) was attributed to this mechanism. In the limit of small $\Gamma=N_e/N_{cr}$ (here 10^{-2}–10^{-3}), the reflectivity for S-polarized light of a plasma-gas interface ($N_e=3.5\times10^{18}$ cm^{-3}) at an angle of incident near 45° is $R_s\approx3\times10^{-6}$, for both internal and external reflections. The increase in electron density at the shock front due to avalanche ionization by the guided pulse may account for the nonlinear increase in the scattered light signal with input intensity. A simple geometric model [48] was used to estimate the fraction of the incident beam reflected into the collection lens L_1, in which a collimated Gaussian beam (spot size w_0) is assumed to be incident on a roughly spherical shock front (radius r_s), which defines the plasma-gas interface. The energy scattered to the collection lens from that area is [37] $E_{sc}\approx E_{in}[\beta^2 e^{-\sqrt{2}\beta^2}]/(4\pi\sqrt{2})R_S\Delta\Omega$, where $\beta=r_s/w_0$, E_{in} is the pulse energy, and $\Delta\Omega$ is the solid angle of the collection lens (for the present arrangement, $\Delta\Omega\approx0.018$ sr). The maximum value $E_{sc}\approx0.015E_{in}\Delta\Omega$ occurs for $\beta^2=1/\sqrt{2}$. For $E_{in}=10$ mJ, the energy scattered to the collection lens is at most $E_{sc}\approx0.01$ nJ, which is of the same order of magnitude as that measured. For comparison, the energy directed into the lens due to Thomson scattering under similar conditions is $E_{TS}\approx(E_{in}/\pi w_0^2)N_e(\delta z\pi w_0^2)r_0^2\Delta\Omega$, where $\delta z\pi w_0^2$ is the scattering volume [49]. Taking $\delta z\approx20$ μm (the pixel size), $E_{sc}/E_{TS}\approx100$.

Although large-angle reflections at the entrance and exit scatter a negligible portion of the input energy (due to the small absolute value of the index discontinuity), additional plasma formation where the lens focus meets the channel entrance can affect the coupling. The ratio E_{in}/E_{out} was observed to decrease above a threshold intensity associated with the appearance of enhanced laser scattering at the entrance of the channel (along with increased fluorescence emission there) (see Fig. 27). Avalanche breakdown at the entrance, seeded by free electrons from the axicon spark, evidently plays a role in limiting the amount of light that can be coupled to the guide. The additional ionization, with its peak on the optical axis, can create a negative plasma lens and scatter the beam, or at least degrade the mode matching. A differential pumping arrangement in which the gas density in the region in front of the channel entrance is limited is currently being tested. Other approaches include using a gas jet or tailoring the channel entrance plasma profile.

Self-focusing at the channel entrance due to the nonlinear refractive index of the atoms and ions is another mechanism that would affect the coupling at high intensities. The threshold power for self-focusing in Xe is approximately 0.4 GW, an order of magnitude larger in peak power than the coupling lens pulse. The nonlinear polarizability for the ground-state ions of this experiment should be lower than that of Xe, due to tighter binding of the electrons. Collisionally excited atoms or ions may have a value of $\chi^{(3)}$ higher than that of the ground-state atoms [20,50]. Such excited atoms and ions may exist at the coupling lens focus, where there are likely many free electrons. However, a pulse that is sufficiently intense rapidly photoionizes these collisionally excited species, due to the lower ionization potential out of the excited state.

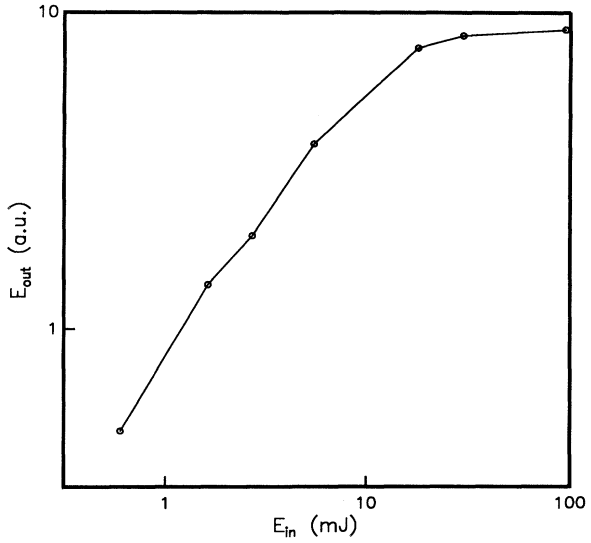

FIG. 27. Relative energy throughput vs input energy (logarithmic scales). Gas: 30-Torr Xe–170–Torr N_2. Pulse energies: $E_1=80$ mJ and $E_2=25$ mJ. Delay: 14 ns. The throughput levels off at an input energy (approximately 15 mJ), which also shows an enhanced level of large-angle scattering at the input.

It was seen above that at short delays, while the plasma channel is in the initial stages of development, the channeled energy is substantially attenuated due to leaky mode radiation. At higher densities and longer delays, when the waveguide supports many modes, the energy throughput is less sensitive to changes in the channel size. For example, in the sequence of multimode images of Fig. 18, the energy throughput was constant to within ±8% throughout the range of delay.

Inverse bremsstrahlung absorption is a possible mechanism for beam attenuation in the channel. For high-intensity pulses, however, inverse bremsstrahlung does not result in a substantial loss of energy. As energy is absorbed, the electron temperature increases, which decreases the absorption rate. For $N_e=N_i=3.3\times10^{18}$ cm^{-3}, $\lambda=1.064$ μm, and $T_e=10$ eV, the linear inverse bremsstrahlung absorption coefficients is [51] 0.62 cm^{-1}. Over a propagation distance of 0.7 cm, this would result

in about 53% of the pulse energy being deposited in the plasma. However, as the pulse energy is absorbed, the electron temperature increases, which decreases the absorption rate. For a temperature of 50 eV, the absorption coefficient is 0.01 cm^{-1}. To raise the electron temperature 10–50 eV would remove only 200 μJ from the beam (assuming a focal volume of 20 μm in radius by 0.7 cm in length). For very high-intensity pulses (where the ponderomotive potential in the laser field satisfies $U_p \gg \kappa_B T_e$), this bleaching effect occurs even before substantial heating occurs, since the quiver energy reduces the electron-ion scattering rate.

Another attenuation mechanism is stimulated Brillouin scattering (SBS), in which the laser beam resonantly couples to ion acoustic waves, causing backscattering. The channeled intensities in this experiment are above the threshold for an exponentially growing level of SBS [52], although an effort to observe stimulated backscattering did not show a measurable amount. This may be due to the pulse duration, since the ion wave must build up from the thermal level of fluctuations during the short pulse.

VI. CONCLUSIONS

The results presented in this paper are a demonstration of the extended, stable channeling of an intense laser beam in plasma. The two-pulse technique demonstrated here should prove very useful in a wide range of applications. The method is more flexible than self-channeling schemes. Since the channel is preformed, the guiding does not rely on a particular channeled intensity, and multiple pulses may even be guided. The method offers more control over the waveguide properties. The delay before pulse injection, the gas composition, the degree of initial plasma heating as well as the length of the channel are all parameters that may be varied. Furthermore, a special property of the plasma waveguide is the wavelength independence of the mode structure. Short wavelength light generated in the channel will also be guided along with a channeled driving pulse. A differential pumping arrangement is currently being tested, which should allow even higher-intensity pulses to be coupled into the guide and permit the exit of short wavelength light into vacuum.

ACKNOWLEDGMENTS

The authors thank T. J. McIlrath for useful discussions. This work is supported by the NSF (Grant Nos. ECS-8858062 and ECS-9224520) and the AFOSR (Grant No. F49620-92-J-0059).

[1] A. McPherson, G. Gibson, H. Jara, U. Johann, T. S. Luk, I. McIntyre, K. Boyer, and C. K. Rhodes, J. Opt. Soc. Am. B **4**, 595 (1987); X. F. Li, A. L'Huillier, M. Feray, L. A. Lompré, and G. Mainfray, Phys. Rev. A **39**, 5751 (1989).

[2] N. H. Burnett and P. B. Corkum, J. Opt. Soc. Am. B **6**, 1195 (1989).

[3] T. Tajima and J. M. Dawson, Phys. Rev. Lett. **43**, 267 (1979).

[4] C. E. Clayton, D. A. Marsh, A. Dyson, M. Everett, A. Lal, W. P. Leemans, R. Williams, and C. Joshi, Phys. Rev. Lett. **70**, 37 (1993).

[5] See, for example, J. Squier, F. Salin, G. Mourou, and D. Harter, Opt. Lett. **16**, 324 (1991); J. D. Kmetec, J. J. Macklin, and J. F. Young, *ibid.* **16**, 1001 (1991); A. Sullivan, H. Hamster, H. C. Kapteyn, S. Gordon, W. White, H. Nathel, R. J. Blair, and R. W. Falcone, *ibid.* **16**, 1406 (1991).

[6] A. B. Borisov, A. V. Borovskiy, V. V. Korobkin, A. M. Prokhorov, O. B. Shiryaev, X. M. Shi, T. S. Luk, A. McPherson, J. C. Solem, K. Boyer, and C. K. Rhodes, Phys. Rev. Lett. **68**, 2309 (1992).

[7] R. W. Falcone, in *X-ray Lasers 1992,* edited by E. E. Fill, IOP Conf. Proc. No. 125 (Institute of Physics and Physical Society, London, 1992).

[8] A. G. Litvak, Zh. Eksp. Teor. Fiz. **57**, 629 (1968) [Sov. Phys. JETP **30**, 344 (1970); C. E. Max, J. Arons, and A. B. Langdon, Phys. Rev. Lett. **33**, 209 (1974).

[9] G. Sun, E. Ott, Y. C. Lee, and P. Guzdar, Phys. Fluids **30**, 526 (1987).

[10] P. Sprangle, E. Esarey, J. Krall, and G. Joyce, Phys. Rev. Lett. **69**, 2200 (1992).

[11] T. M. Antonsen and P. Mora, Phys. Rev. Lett. **69**, 2204 (1992).

[12] A. Sullivan, S. Gordon, H. Hamster, R. W. Falcone, and H. Nathel, in *OSA Proceedings on Shortwavelength V: Physics with Intense Laser Pulses,* edited by M. D. Perry and P. B. Corkum (Optical Society of America, Washington, DC, 1993), p. 40.

[13] P. Monot, T. Auguste, L. A. Lompré, G. Mainfray, and C. Manus, J. Opt. Soc. Am. B **9**, 1579 (1992).

[14] J. H. Mcleod, J. Opt. Soc. Am. **44**, 592 (1954).

[15] G. A. Askar'yan and N. M. Tarasova, Pis'ma Zh. Eksp. Teor. Fiz. **20**, 277 (1974) [JETP Lett. **20**, 123 (1974)].

[16] L. C. Johnson and T. K. Chu, Phys. Rev. Lett. **32**, 517 (1974); T. K. Chu and L. C. Johnson, Phys. Fluids **18**, 1460 (1975).

[17] G. M. Molen, M. Kristiansen, and M. O. Hagler, Appl. Phys. Lett. **23**, 601 (1973).

[18] N. A. Amherd and G. C. Vlases, Appl. Phys. Lett. **24**, 93 (1973).

[19] C. G. Durfee III and H. M. Milchberg, Phys. Rev. Lett. **71**, 2409 (1993).

[20] F. V. Bunkin, I. K. Krasyud, V. M. Marchenko, P. P. Pashinin, and A. M. Prokhorov, Zh. Eksp. Teor. Fiz. **60**, 1326 (1971) [Sov. Phys. JETP **33**, 717 (1971)].

[21] M. H. Key, D. A. Preston, and T. P. Donaldson, J. Phys. B **3**, L88-92 (1970).

[22] X. Liu and D. Umstadter, in *OSA Proceedings on Shortwavelength V: Physics with Intense Laser Pulses* (Ref. [12]), Vol. 17, p. 45.

[23] L. Sedov, *Similarity and Dimensional Methods in Mechanics* (Academic, New York, 1959).

[24] N. W. Krall and A. W. Trivelpiece, *Principles of Plasma*

Physics (San Francisco Press, San Francisco, 1986), p. 90.
[25] M. V. Ammosov, N. B. Delone, and V. P. Krainov, Zh. Eksp. Teor. Fiz. **91**, 2008 (1986) [Sov. Phys. JETP **64**, 1191 (1986)].
[26] Yu. P. Raizer, *Laser-Induced Discharge Phenomena* (Consultants Bureau, New York, 1977).
[27] S. C. Brown, *Basic Data of Plasma Physics, 1966* (Wiley, New York, 1967), p. 22.
[28] For references to a number of high-field bremsstrahlung calculations, see T. P. Hughes, *Plasmas and Laser Light* (Wiley, New York, 1975).
[29] R. W. P. McWhirter, in *Plasma Diagnostic Techniques,* edited by R. H. Huddlestone and S. L. Leonard (Academic, New York, 1965).
[30] Ya. B. Zel'dovich and Yu. P. Raizer, *Physics of Shock Waves and High-Temperature Hydrodynamic Phenomena* (Academic, New York, 1967).
[31] S. C. Brown, *Basic Data of Plasma Physics, 1966* (Ref. [27]), p. 46.
[32] C. G. Durfee III, J. Lynch, and H. M. Milchberg, Opt. Lett. **19**, 1937 (1994).
[33] H. M. Milchberg, J. Lynch, and C. G. Durfee, J. Opt. Soc. Am. B (to be published).
[34] H. J. Lehmeier, W. Leupacher, and A. Penzkofer, Opt. Commun. **56**, 67 (1985).
[35] A. Seigman, *Lasers* (University Science Books, Mill Valley, CA, 1986), p. 647.
[36] A. W. Snyder and J. D. Love, *Optical Waveguide Theory* (Chapman and Hall, London, 1983).
[37] C. G. Durfee III, Doctoral Dissertation, University of Maryland, 1994.
[38] A. Yariv, *Quantum Electrons,* 3rd ed. (Wiley, New York, 1989).
[39] M. D. Feit and J. A. Fleck, Jr., Appl. Phys. Lett. **28**, 121 (1976); J. A. Fleck, Jr., J. R. Morris, and M. D. Feit, Appl. Phys. **10**, 129 (1976).
[40] R. Tremblay, Y. D'Astous, G. Roy, and M. Blanchard, Opt. Commun. **28**, 193 (1979).
[41] O. G. Ivanov, R. I. Okunev, L. N. Pakhomov, V. Yu. Petrun'kin, L. Ya. Polonsky, and L. N. Pyatnitsky, Zh. Tekh. Fiz. **57**, 2012 (1987) [Sov. Phys. Tech. Phys. **32**, 1212 (1987)].
[42] V. V. Korobkin, L. Ya. Polonsky, V. P. Poponin, and L. N. Pyatnitsky, Kvant. Elektron. (Moscow) **13**, 265 (1986) [Sov. J. Quantum Electron. **16**, 178 (1986)].
[43] A. L'Huillier, L. A. Lompre, G. Mainfray, and C. Manus, J. Phys. B **16**, 1363 (1983).
[44] L. N. Pyatnitsky, L. Ya. Polonsky, and M. I. Uvaliev, Rev. Sci. Instrum. **62**, 1139 (1991).
[45] R. Tremblay, Y. D'Astous, G. Roy, and M. Blanchard, Opt. Commun. **28**, 193 (1979).
[46] V. V. Korobkin, L. Ya. Margolin, L. Ya. Polonsky, and L. N. Pyatnitsky, Kvant. Elektron. (Moscow) **16**, 1214 (1989) [Sov. J. Quantum Electron. **19**, 1214 (1990)].
[47] N. E. Andreev, V. M. Batenin, L. Ya. Margolin, L. Ya. Polonsky, L. N. Pyatnitsky, Yu. A. Aristov, A. I. Zykov, and N. M. Terterov, Zh. Tekh. Fiz. **15**, 83 (1989) [Sov. Tech. Phys. Lett. **15**, 116 (1989)].
[48] N. Ahmad, B. C. Gale, and M. H. Key, J. Phys. B **2**, 403 (1969).
[49] J. Sheffield, *Plasma Scattering of Electromagnetic Radiation* (Academic, New York, 1975).
[50] M. H. Key, D. A. Preston, and T. P. Donaldson, J. Phys. B **3**, L88-92 (1970).
[51] T. P. Hughes, *Plasmas and Laser Light* (Ref. [28], p. 44).
[52] W. L. Kruer, *Physics of Laser-Plasma Interactions* (Addison-Wesley, Reading, MA, 1988).

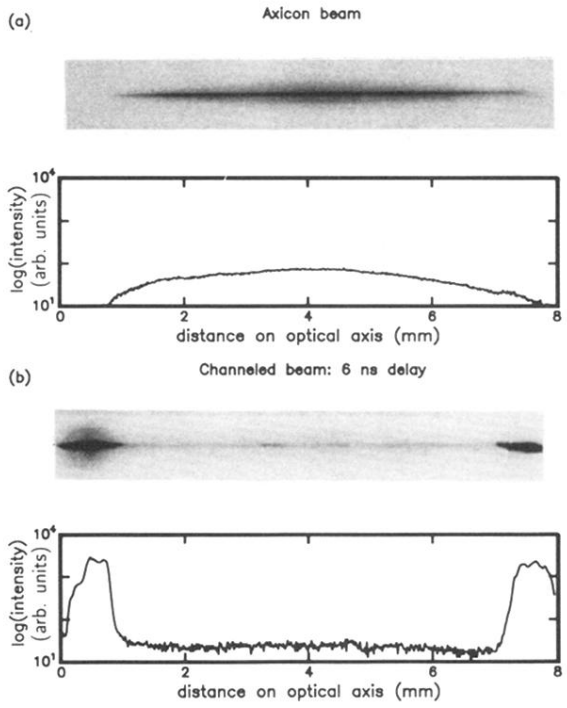

FIG. 14. Images and axial lineouts of scattered laser light from the axicon focal region. Gas: 30-Torr Xe–95-Torr N_2. Pulse energies: $E_1 = 160$ mJ and $E_2 = 15$ mJ. (a) Axicon beam alone. (b) Channeled beam injected after a 6-ns delay. The background is subtracted from each.

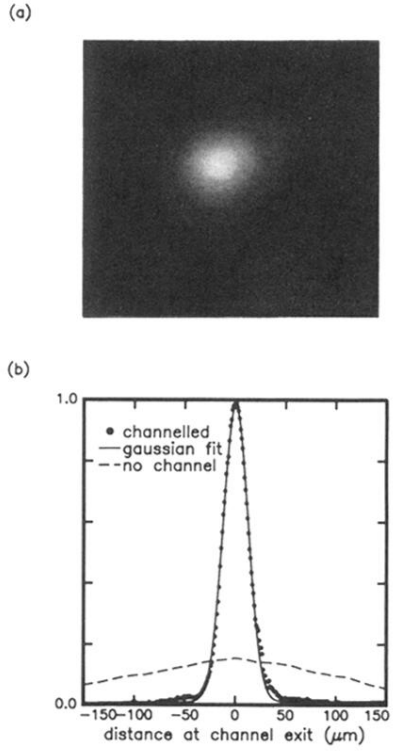

FIG. 15. (a) Mode profile at channel exit. The beam is focused at the entrance of the channel and couples to low-order channel mode(s). Gas: 30-Torr Xe–170-Torr N_2; pulse energies: $E_1 = 100$ mJ and $E_2 = 25$ mJ; delay: 12 ns. (b) Lineout of this image, where the least squares fit to a Gaussian gives a FWHM of 25 μm. The dashed line shows the size of the beam at this focal plane when the axicon spark is not present.

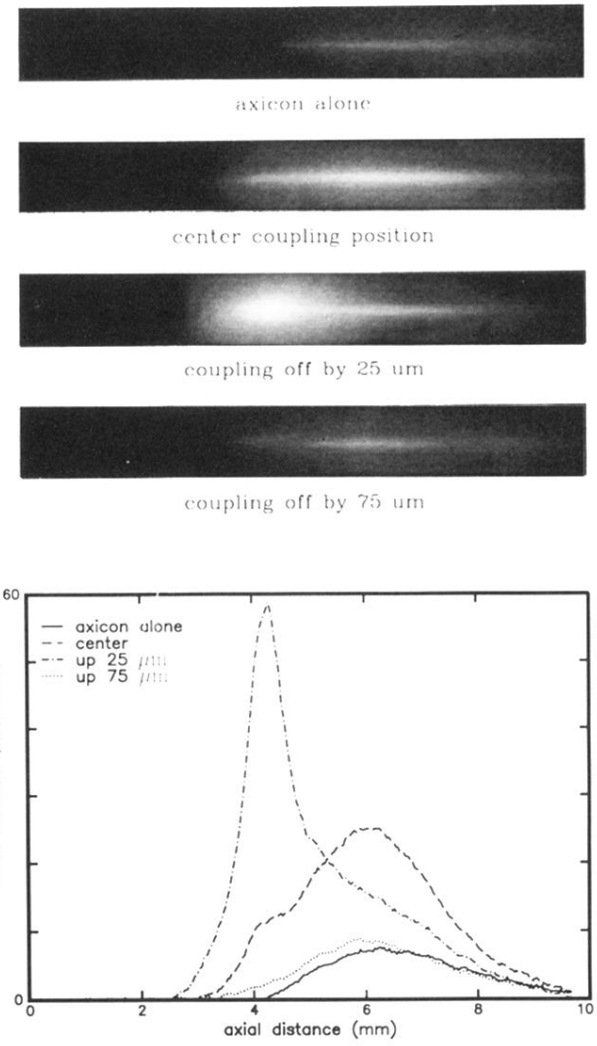

FIG. 18. Images and lineouts of fluorescence from the axicon focal region as input coupling is detuned. Gas: 30-Torr Xe. Pulse energies: $E_1 = 145$ mJ and $E_2 = 40$ mJ. Delay: 15 ns.

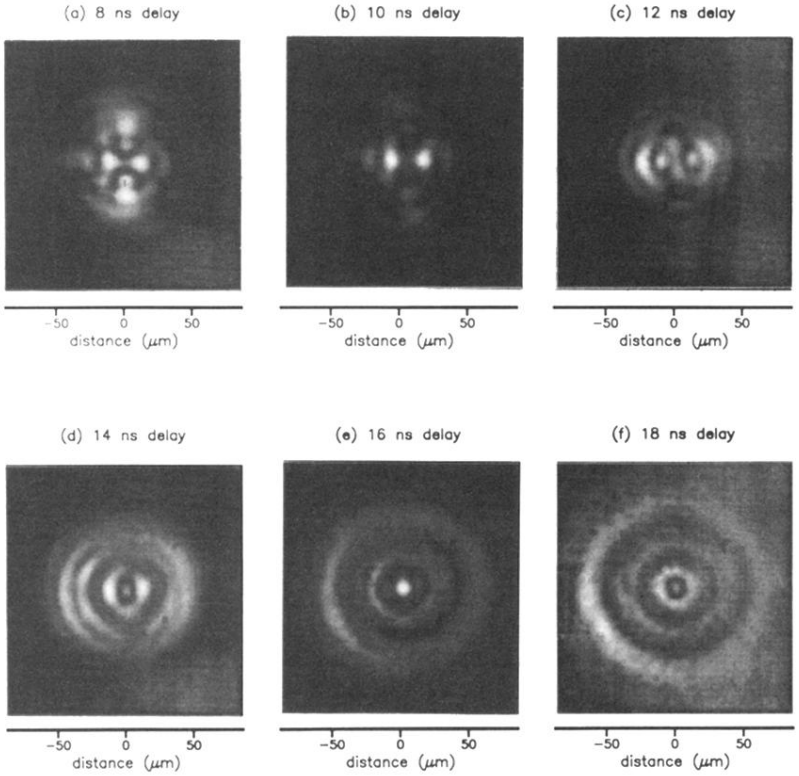

FIG. 19. Exit modes for various delays. The input beam was focused 1 mm in advance of the channel entrance, forcing it to couple to high order modes. Gas: 30-Torr Xe–170-Torr N_2. Pulse energies: $E_1 = 160$ mJ and $E_2 = 25$ mJ.

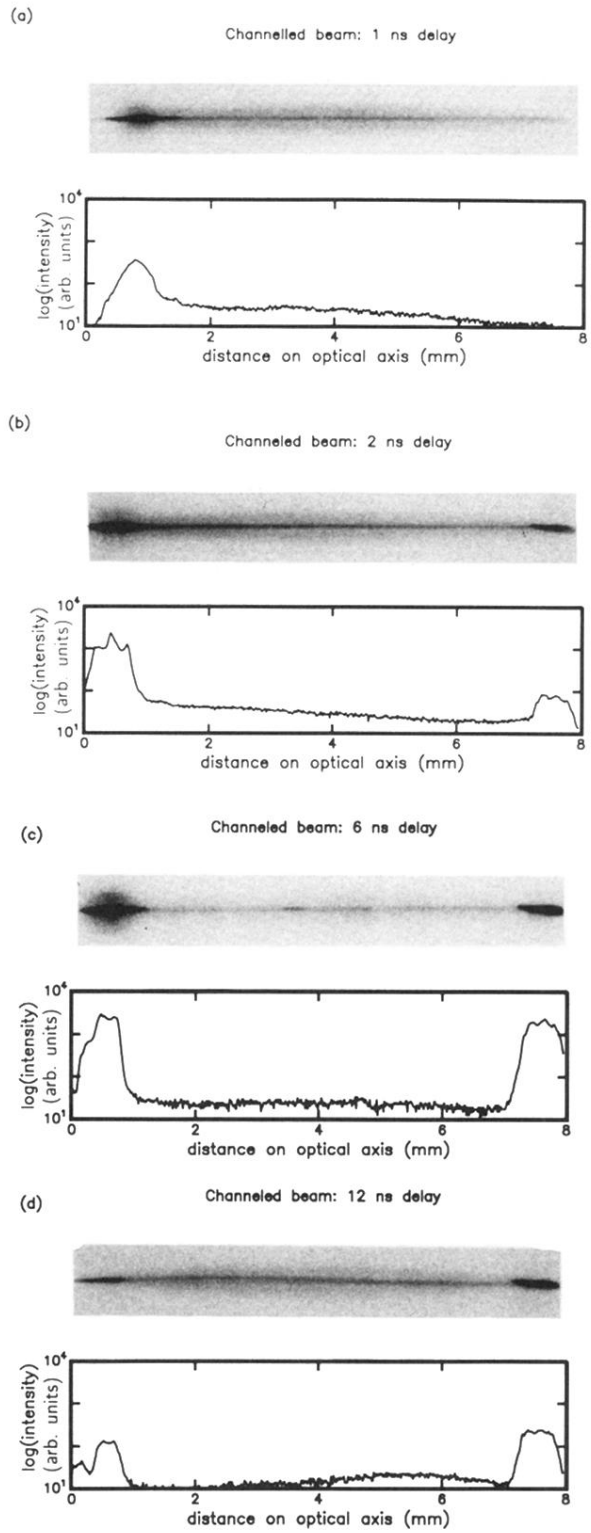

FIG. 23. Images and axial lineouts of scattered laser light, showing reduction in leaky mode attenuation at longer delay. Laser is incident from left. Gas: 30-Torr Xe–95-Torr N_2. Pulse energies: $E_1 = 160$ mJ and $E_2 = 15$ mJ.

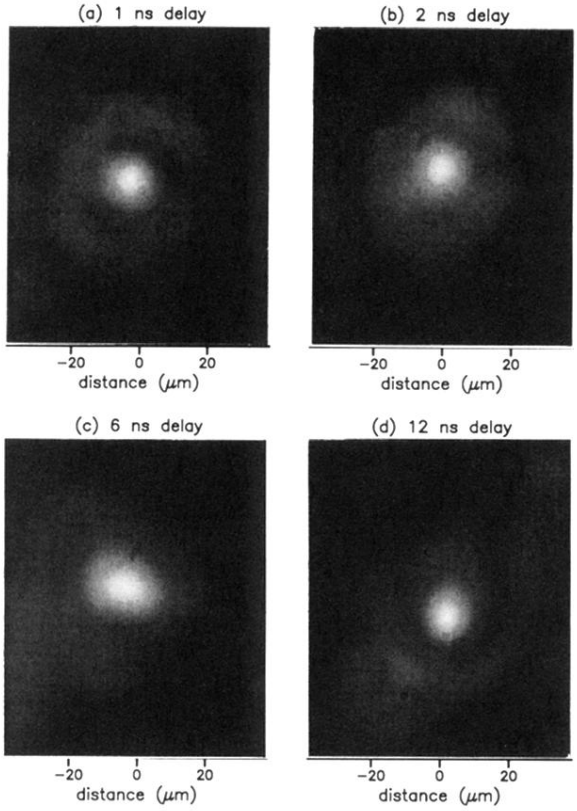

FIG. 24. Exit mode images for the data shown in Fig. 23. Relative throughput: (a) 0.21; (b) 0.33; (c) 0.82; and (d) 1.0.

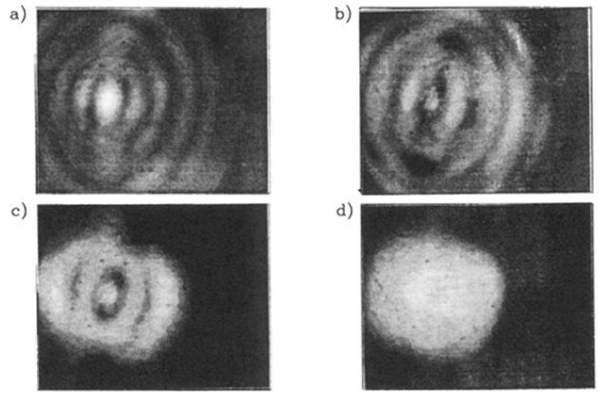

FIG. 9. Axial scattering images of probe pulse. Gas: 30-Torr Ar. Pulse energies: $E_1 = 70$ mJ and $E_2 = 10$ mJ. Probe pulse delays: (a) 0.2 ns, (b) 1.1 ns, (c) 2.9 ns, and (d) 5.9 ns.